Biology Direct

RESEARCH Open Access

Circulating extracellular vesicles regulate ELAVL1 by delivering miR-133a-3p which affecting NLRP3 mRNA stability inhibiting PANoptosome formation

Deliang Wang[1†], Zheng Dai[2†], Lu Jiang[1*] and Ke Liu[1*]

Abstract

Background In the quest to elucidate novel therapeutic strategies for myocardial injury, recent investigations have underscored the pivotal roles played by circulating extracellular vesicles (EVs) in intercellular communication.

Method EVs were extracted from individuals who had experienced AMI-EVs and those who were N-EVs. To assess the impact of circulating EVs on cardiomyocyte and endothelial cell proliferation, apoptosis, migration, and tube formation, a range of in vitro assays such as CCK8, EdU assays, flow cytometry, wound healing assays and angiogenesis assays were conducted. Differentially expressed miRNAs in EVs were validated using microarray analysis and real-time PCR. Through bioinformatics analysis, ELAVL1 was identified as a potential downstream target of miR-133a-3p. This finding was further confirmed by conducting dual-luciferase reporter assay and RNA co-immunoprecipitation experiments. To investigate the regulatory effects of circulating EVs from various sources on myocardial injury and PANoptosis, an animal model of ischemia-reperfusion-induced myocardial injury was established.

Result Our findings revealed that circulating EVs effectively deliver miR-133a-3p to target cells, where it binds to ELAVL1, leading to a decrease in NLRP3 mRNA stability. This reduction in NLRP3 mRNA stability subsequently inhibits the assembly of the PANoptosome, a multi-protein complex implicated in PANoptosis. As a result, we observed a significant mitigation of PANoptosis in our myocardial injury models, demonstrating the protective role of miR-133a-3p against excessive cell death.

Conclusion The present study underscores the regulatory role of circulating EV-delivered miR-133a-3p in modulating PANoptosis through ELAVL1-mediated NLRP3 mRNA stabilization. This mechanism represents a potential therapeutic target for attenuating myocardial injury by suppressing PANoptosis.

Keywords Extracellular vesicles, ELAVL1, PANoptosis, Myocardial injury, miR-133a-3p

[†]Deliang Wang and Zheng Dai contributed equally to this work.

*Correspondence:
Lu Jiang
jlzl213@163.com
Ke Liu
liuke905310@163.com

[1]Department of Cardiac Surgery, Sichuan Provincial People's Hospital, University of Electronic Science and Technology of China, Chengdu, Sichuan 610072, China
[2]Department of Emergency Medicine, Sichuan Provincial People's Hospital, University of Electronic Science and Technology of China, Chengdu, Sichuan 610072, China

Introduction

Acute myocardial infarction (AMI) is currently the leading cause of death and disability in humans [1]. Current studies have shown that timely reperfusion therapy (such as percutaneous coronary intervention, coronary artery bypass grafting and early thrombolysis) is the most effective way to save patients with AMI [2]. However, reperfusion therapy is often accompanied by a series of cardiac-related adverse events such as myocardial stunning, reperfusion arrhythmia, and microvascular dysfunction, resulting in further aggravation of myocardial injury, a phenomenon known as myocardial ischemia-reperfusion injury (MIRI) [3].

Extracellular vesicles (EVs) were goblet lipid bilayer membrane vesicles with a diameter of 30–150 nm, which are released by various types of eukaryotic cells into extracellular fluids such as blood, cerebrospinal fluid, saliva, and bile [4]. It constitutes extensive communication networks implicated in the regulation of various processes such as development, immunity, tissue balance, tumors, and neurodegenerative disorders. Thorough investigations have revealed that EVs harbor a significant abundance of miRNAs which can exert crucial regulatory functions in myocardial injury via autocrine and paracrine mechanisms.

MiRNAs are a class of endogenous, non-coding single-stranded small RNAs of about 22 nucleotides in length [5]. They are the main factors regulating gene transcription and are of great significance in exosome-mediated intercellular communication. Exosomes transport and release miRNAs to target cells through plasma membrane fusion, cell pinocytosis, and specific receptor-dependent pathways [4]. The main function of EVs-miRNAs is to participate in the negative regulation at the target gene level. A single miRNA can regulate multiple target gene loci, and a single mRNA can also be regulated by multiple miRNAs [6]. If the miRNAs exhibit complete complementarity with the target mRNAs, degradation of the target mRNAs occurs. Recent investigations have revealed that differential expression of EVs-miRNAs in patients suffering from cardiovascular disease can exert control over transcription and translation processes of diverse genes, thereby intervening in pathophysiological mechanisms such as inflammation, cell proliferation, and apoptosis. Consequently, they are progressively emerging as a pivotal therapeutic target for cardiovascular disease treatment [7].

PANoptosis, not merely a recently acknowledged form of pro-inflammatory programmed cell death, but also an emergent concept that highlights the crosstalk and coordination among three cell death modalities– pyroptosis, apoptosis, and necroptosis [8]. This unique process is driven by a multi-protein complex known as the PANoptosome, which facilitates the crosstalk and regulation between these processes [9]. Recent studies have unveiled that the PANoptosome harbors pivotal molecules essential for pyroptosis, apoptosis, and necroptosis, including GSDMD, Caspase1, Caspase3, Caspase8, RIPK1, and RIPK3, enabling the activation and execution of all three pathways [10]. It is hypothesized that this conceptual complex forms a flexible scaffold capable of recruiting the core components of distinct cell death modes to execute cell demise [11]. Notably, NLRP3 plays a critical role indispensable for the activation of all three pathways [12]. Therefore, PANoptosis can further exacerbate inflammation and induce myocardial cell death, highlighting the significance of inhibiting PANoptosis as a crucial strategy for myocardial protection and mitigation of AMI injury. However, there is still a need for further investigation into the regulatory mechanisms underlying PANoptosis in AMI injury.

Therefore, this study aimed to investigate the therapeutic effects of EVs derived from various sources on myocardial injury. Specifically, we examined how miR-133a-3p modulates the impact of cardiomyocyte PANoptosis on exosome-mediated treatment of myocardial injury through its regulation of ELAVL1.

Materials and methods

Clinical samples

The AMI patients included in this study were recruited from the Sichuan Provincial People's Hospital. The diagnosis of AMI was based on the criteria outlined in the 2017 ESC Guidelines. For the control group, volunteers who visited the hospital for a physical examination during the same time period were selected. There were no significant differences observed in demographic characteristics such as age, gender, and weight between healthy individuals and those with AMI. All case information is presented in Supplementary Table 1. All participants provided informed consent after understanding the study protocol, which had been approved by the Ethics Committee of Sichuan Provincial People's Hospital.

Isolation of serum EVs

After the samples were collected, they were divided into aliquots of 500μL per tube on ice, and the insufficient part was supplemented to 500μL with 1×PBS. Subsequently, cell debris was removed by centrifugation, and the sample was transferred to a 1.5-ml centrifuge tube and centrifuged at 3000 ×g for 10 min at 4 ℃. On further removes impurities to pieces, the centrifugal clear liquid transferred to the new tube, in 4 ℃, and 12,000 g under the conditions of the centrifugal for 10 min. Next, 400μL of precooled Solution A was added to the 500μL blood sample and immediately mixed through a vortex oscillator for 30 s, followed by centrifugation again at 12,000×g for 20 min to remove miscellaneous proteins.

After that, the supernatant was transferred to a new tube, and 120μL of Solution B was added, vortexed and shaken again for 1 min, and then left at 4 ℃ for at least 30 min. Next, the mixture was removed and centrifuged at 12,000×g for 15 min at 4 ℃, and the supernatant was discarded, retaining the exosomes-rich precipitate. Centrifugation was repeated for 2 min to further remove the supernatant. After that, the centrifuged precipitate was resuspended with an appropriate amount of 1×PBS and transferred to a new 1.5mL centrifuge tube. Finally, the centrifuge tube containing the resuspension was centrifuged at 12,000×g for 2 min, retaining the supernatant, which was rich in exosome particles. To purify exosomes, the harvested crude exosomes were transferred to the upper chamber of an ExosomePurification Filter (EPF column) and centrifuged at 3 000×g for 10 min at 4℃. The liquid at the bottom of the EPF column was collected as the purified exosomes. The purified exosomes should be packaged and frozen in a low-temperature refrigerator at -80℃ for subsequent experiments.

Particle diameter

The determination of particle diameter and zeta potential was carried out using the Zetasizer Nano instrument (manufacturer: Malvern Panalytical, location: Westborough, MA), under conditions of an EV protein concentration ranging from 0.2 to 0.5 mg/mL, a temperature of 25 °C, and a scattering angle of 173°. The particle size distribution was measured in 1x PBS, whereas the zeta potential was determined in 10 mM HEPES buffer (pH 7.4). All experiments were conducted in triplicate, and the data are presented as the mean ± standard deviation (SD) of the triplicate measurements.

TEM

For TEM, EV samples at ~2.0E + 11 p/mL were transferred to a 200-mesh Formvar and carbon-coated copper grid (Ted Pella) and incubated for 1 min. After adsorption, the grids were rinsed with water and the excess solution was wicked away. The grids were then stained with a 1% solution of uranyl acetate for ~30 s. After staining, the excess solution was wicked away and the grids were allowed to dry. The negatively stained samples were analyzed with a FEI Morgagni (Hillsboro) electron microscope operating at 80 kV.

MiRNA microarray analysis

After the normalization and log2 transformation of the microarray data, limma, an R software package, was used to identify DEGs between the AMI-EVs and N-EVs. The selection criterion for DECs was a p of < 0.05 and a| log2(fold change)| > 0. The Robust rank aggregation package in R was used to integrate and rank all harvested DECs with the criterion of $p < 0.05$. The RRA method was based on the theory that genes in each experiment were randomly ordered. For the genes ranking higher in the experiment, the possibility of differential expression is inversely proportional to the value of p. R software was used to draw the volcano plot.

Cell culture

The AC16 human cardiomyocytes, HUVEC human umbilical vein endothelial cells, and HEK-293T cells were obtained from a Chinese company called Procell biological. All cell lines were cultured in DMEM medium supplemented with 10% fetal bovine serum (FBS) and 1% dual antibiotics (penicillin and streptomycin). The cells were incubated under the conditions of 37 ℃ and 5% CO_2.

Flow cytometry

The cells were harvested and subjected to the staining protocol provided by the Annexin V-FITC/PI apoptosis detection kit. Flow cytometry was employed to visualize apoptotic events, and subsequently, the rate of apoptosis was determined.

Cell counting kit-8 (CCK8)

The cells from each treatment group were transformed into a suspension of individual cells, which were then introduced into a 96-well culture plate at a density of 5×10^3 cells per well. The plate was incubated in a CO_2 incubator at 37 °C for 24 h, followed by the addition of CCK8 working solution to each well. After placing the plate in the incubator for an additional 4 h, the optical density was measured using a microplate reader.

Dual-luciferase reporter gene assay

ELAVL1 wild-type (ELAVL1-WT) and mutant (ELAVL1-MUT) plasmids containing miR-133a-3p binding sequences were constructed, and the above plasmids were co-transfected with miR-133a-3p NC and miR-133a-3p mimic, respectively. In HEK293 cells, transfection was carried out according to the manufacturer's requirements of Lipofectamine 3000 transfection reagent. After 48 h, the cells were collected and lysed. The luciferase activity of each group of cells was detected by the dual-luciferase detection kit, and the detection was carried out according to the requirements of the kit.

Quantitative real-time PCR (qRT-PCR)

Total RNA was extracted from myocardial tissue and cells using TRIzol reagent (Life Technologies). cDNA synthesis was performed using M-MLV Reverse Transcriptase (Takara). The specific products were quantitatively amplified by PCR using the TransStart Green Q-PCR SuperMix Kit (TransGen). β-actin served as a

normalization control. The primer sequences are provided in Supplementary Table 2.

Western blot (WB)

The cells and EVs were lysed using a lysis buffer containing radioimmunoprecipitation, and the supernatant was measured using a BCA protein quantification kit. Subsequently, SDS-PAGE gel electrophoresis was conducted, followed by transferring the proteins to PVDF membranes at a current of 90 mA. Prior to adding primary antibodies CD9 (1:2,000, ab307085, abcam, USA), TSG101 (1:2,000 ab125011, abcam, USA), CD63 (1:1,000 ab315108, abcam, USA), VEGFA (1:1,000 ab46154, abcam, USA), ELAVL1 (1:2000 ab170193, abcam, USA) and GAPDH (1:1000, ab8245, abcam, USA) which were incubated overnight at 4 °C., the membrane was blocked with skim milk containing 5%. On the following day, horseradish peroxidase-conjugated secondary antibody goat anti-rabbit IgG (diluted at 1:2,000) was applied to the membrane for an hour at room temperature. Finally, chemi-enhanced luminescence reagents were used for visualizing the proteins which were then analyzed on a Bio-Rad digital imaging system.

EdU assays

After completing the EdU labeling process, the culture medium was removed and replaced with 1 ml of a 4% paraformaldehyde solution for fixation at room temperature for 15 min. The fixative was then discarded, and the cells were rinsed three times using 1 ml of washing solution per well. Subsequently, each well was exposed to 1 ml of PBS containing 0.3% TritonX-100 for a duration of 15 min at room temperature. Following this step, a volume of 0.5 ml Click Reaction was added to every well and gently agitated to ensure uniform coverage over the samples. The plate was incubated in darkness at room temperature for a period of 30 min. After removing the washing solution, each well received an addition of 1 ml of DAPI solution (at a concentration equivalent to that denoted as '1X') and further incubation in darkness at room temperature for approximately ten minutes. Any remaining liquid on the slide surface was dried using absorbent paper before sealing it with an antifluorescence quencher compound. Finally, images were observed and collected under a fluorescence microscope.

Angiogenesis assay

Refrigerate the matrigel gel at 4 °C overnight until it melts, pre-chill the 24-well plate and pipette tips, add 200μL per well to the pre-cooled 24-well plate, gently centrifuge at a low speed to eliminate any trapped air bubbles, and incubate at a temperature of 37 °C for a duration of 30–60 min. Obtain HUVEC cells that have been grouped and treat them with 0.25% trypsin for digestion. Create a suspension of single cells using serum-free medium. Inoculate the cells onto the precoated matrigel in each well of a 24-well plate following an even distribution of approximately 1×10^5/cell per well. After incubation under conditions of 37℃ and saturated humidity with CO_2 concentration maintained at around 5%, observe angiogenesis in each treatment group using a microscope.

Wound assay

HUVECs were cultured in six-well plates at a density of 3×10^5 cells per well. Once the cells had adhered, a 200 μL pipette tip was used to create scratches on the HUVEC monolayer. Subsequently, the culture medium was replaced with serum-free ECM medium supplemented with H_2O_2 (200μmol/L) and either PBS, N-EVs (50 μg/mL), or AMI-EVs (50 μg/mL). After incubating for 12 h, cell migration was evaluated using inverted fluorescence microscopy. The acquired images were analyzed using ImageJ software to quantify the area covered by migrated cells.

RNA immunoprecipitation

RNA Binding Protein Immunoprecipitation Assays were performed on PASMCs using the Magna RIP kit from Millipore (17–700) according to the protocol provided. A ELAVL1 specific antibody from Millipore and rabbit IgG purified antibodies (provided in the kit) have been used. The purified RNA was subjected to RT-PCR using specific primers for the binding site of ELAVL1 motif in 3'UTR region of NLRP3.

Establishment of MI model and exosome injection

Our animal study adheres to the guidelines outlined in the Guide for the Care and Use of Laboratory Animals published by the National Institutes of Health (NIH, Bethesda, MD, USA), and has been approved by the Institutional Animal Care and Use Committee of Sichuan Provincial People's Hospital. Male Sprague Dawley rats, aged 6–8 weeks, were sourced from the Animal Core Facility of Sichuan Provincial People's Hospital (Sichuan, China). Under intraperitoneal anesthesia induced by sodium pentobarbital (50 mg/kg), the rats were intubated orally and connected to a ventilator. Following secure positioning, a left thoracotomy was executed under sterile conditions between the third and fourth intercostal spaces, followed by ligation of the left anterior descending coronary artery approximately 1.5 mm below the lower edge of the left auricle. Upon successful creation of the myocardial infarction (MI) models, 50 μg of exosomes were evenly distributed and injected into four sites around the infarction border. Postoperatively, carprofen (10 mg/kg) was administered to manage pain and ensure the animals did not endure unnecessary suffering. Both

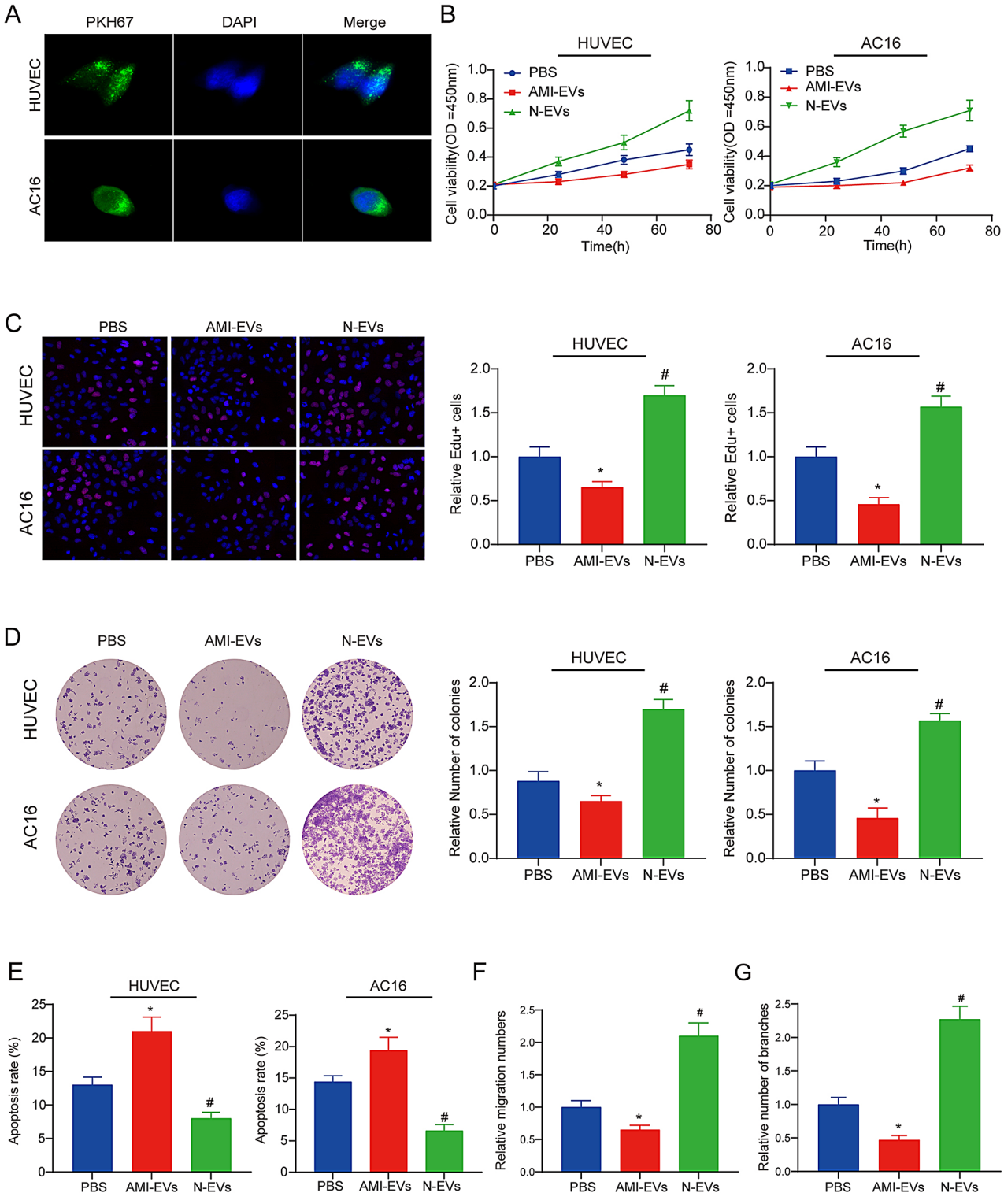

Fig. 1 (See legend on next page.)

the surgical procedures and follow-up analyses were conducted in a blinded manner regarding the intervention.

Cardiac function assessment

14 days and 28 days post-exosome treatment, cardiac function was assessed via transthoracic echocardiography using the Vevo 2000 high-resolution micro-imaging

(See figure on previous page.)

Fig. 1 Regulatory effects of EVs from different sources on cardiomyocytes and endothelial cells. (**A**) PKH67-labeled exosomes were used to investigate the cellular uptake of exosomes after 24 h of co-culture, and immunofluorescence was employed for detection. Legend: To investigate the cellular uptake of exosomes from different sources, PKH67 fluorescent dye was used to label the exosomes. After a 24-hour co-culture with HUVEC or AC16 cells, the intracellular fluorescence signals were observed using immunofluorescence microscopy to assess the efficiency of exosome uptake. The figure shows the uptake of exosomes from different sources, including the negative control group (no exosomes added) and the positive control group (PKH67-labeled exosomes added). Scale bar: 10 μm. (**B**) The cell proliferation ability of EVs derived from different sources on HUVEC and AC16 cells was assessed using CCK8 assay. Legend: The CCK8 assay was used to evaluate the impact of EVs from different sources on the proliferation of HUVEC and AC16 cells. The results are expressed as absorbance values at 450 nm, reflecting the degree of cell proliferation. (**C**) EdU assay was performed to evaluate the cell proliferation ability of EVs from various sources on HUVEC and AC16 cells. Legend: The EdU assay was used to assess the impact of EVs from different sources on the proliferation of HUVEC and AC16 cells. In this assay, EdU is incorporated into newly synthesized DNA during cell replication, and the proportion of EdU-positive cells is observed under a fluorescence microscope to reflect cell proliferation. Scale bar: 100 μm. (**D**) Colony-formation assay was performed to evaluate the cell proliferation ability of EVs from various sources on HUVEC and AC16 cells. Legend: The colony-formation assay was used to evaluate the impact of EVs from different sources on the proliferation of HUVEC and AC16 cells. Cells were seeded in culture dishes, treated with different sources of EVs, and cultured for 10–14 days before counting the number of colonies formed. Scale bar: 100 μm. (**E**) Flow cytometry analysis was conducted to determine the apoptosis rate in different treatment groups. Legend: Flow cytometry was used to analyze the apoptosis rate in different treatment groups. Annexin V-FITC/PI double staining was used to detect apoptosis, showing the proportions of early apoptotic (Annexin V + PI-), late apoptotic (Annexin V + PI+), and necrotic cells (Annexin V- PI+). (**F**) The impact of EVs on the migratory capacity of HUVEC cells was evaluated through a wound healing assay. Legend: The wound healing assay was used to evaluate the impact of EVs from different sources on the migratory capacity of HUVEC cells. A scratch was made in a monolayer of cells, and different sources of EVs were added. Photos of the scratch healing process were taken at 0 h and 24 h. (**G**) Angiogenesis assays were conducted to assess the effects of AMI-EVs and N-EVs on tube formation capability. Legend: Angiogenesis assays were used to assess the effects of AMI-EVs and N-EVs on the tube formation capability of HUVEC cells. Cells were seeded on Matrigel, treated with different sources of EVs, and cultured for 6 h before observing and photographing the tube formation. Scale bar: 100 μm. Statistical significance was determined by comparing with PBS group (*$P < 0.05$), as well as AMI-EVs group (#$P < 0.05$)

system. Rats were anesthetized with sodium pentobarbital (50 mg/kg) through intraperitoneal injection and positioned supinely on a heated platform. The internal dimensions of the left ventricle (LV) were measured from M-mode recordings obtained with a 30 MHz transducer in the short-axis view. Left ventricular ejection fraction (LVEF) and left ventricular fractional shortening (LVFS) were subsequently calculated using the Vevo 2000 workstation software.

Masson trichrome staining

To assess fibrosis, paraffin-embedded heart tissue sections were stained with Masson's trichrome. The extent of infarction was quantified as the mean ratio of fibrotic area to total ventricular area. Microscopic images were captured using a scanning electron microscope (SU8010, Japan) and analyzed with ImageJ software.

Immunofluorescence

Following the procedure described previously, heart tissues were harvested, fixed in 4% paraformaldehyde (PFA), paraffin-embedded, and sectioned. For immunofluorescence analysis, sections were incubated with primary antibodies targeting ELAVL1 (1:200, ab7388, Abcam, Cambridge, UK) and Actin (1:200, A2066, Sigma-Aldrich). Nuclei were counterstained with DAPI.

Statistical analysis

Statistical analysis was conducted using GraphPad software. The measurement data were presented as mean ± standard deviation (x ± s). Analysis of variance was employed, and pairwise comparisons were performed using the Tukey test. A significance level of $P < 0.05$ was considered statistically significant.

Result

Characterization of EVs of different origins

Firstly, circulating blood exosomes were extracted from both the control and AMI groups, and the concentration of exosomes and total protein was examined. The results showed no statistically significant difference in EVs between the two groups (Supplementary Fig. 1A-B). Additionally, WB detection of CD63, CD9 and TSG101 indicated that the purity and concentration of exosomes from both sources were similar (Supplementary Fig. 1C). TEM showed that EVs derived from normal individuals and AMI patients exhibited a typical cup-shaped morphology with a size of approximately 100 nm (Supplementary Fig. 1D). Additionally, the particle size and concentration of EVs from both groups were similar (Supplementary Fig. 1E). These findings suggest that the exosomes isolated from both the control and AMI groups are of comparable quality and quantity, which is essential for subsequent functional studies and comparisons.

Regulatory effects of EVs from different sources on cardiomyocytes and endothelial cells

This study explored the impact of extracellular vesicles (EVs) from different sources on two cell types—AC16 (a human cardiac myocyte cell line) and HUVEC (human umbilical vein endothelial cells) through a series of experiments. Initially, PKH67 was employed to label non-source EVs for validation of their ability to enter AC16 and HUVEC cells (Fig. 1A). Subsequently, the impact of co-culturing EVs from different sources on cell viability

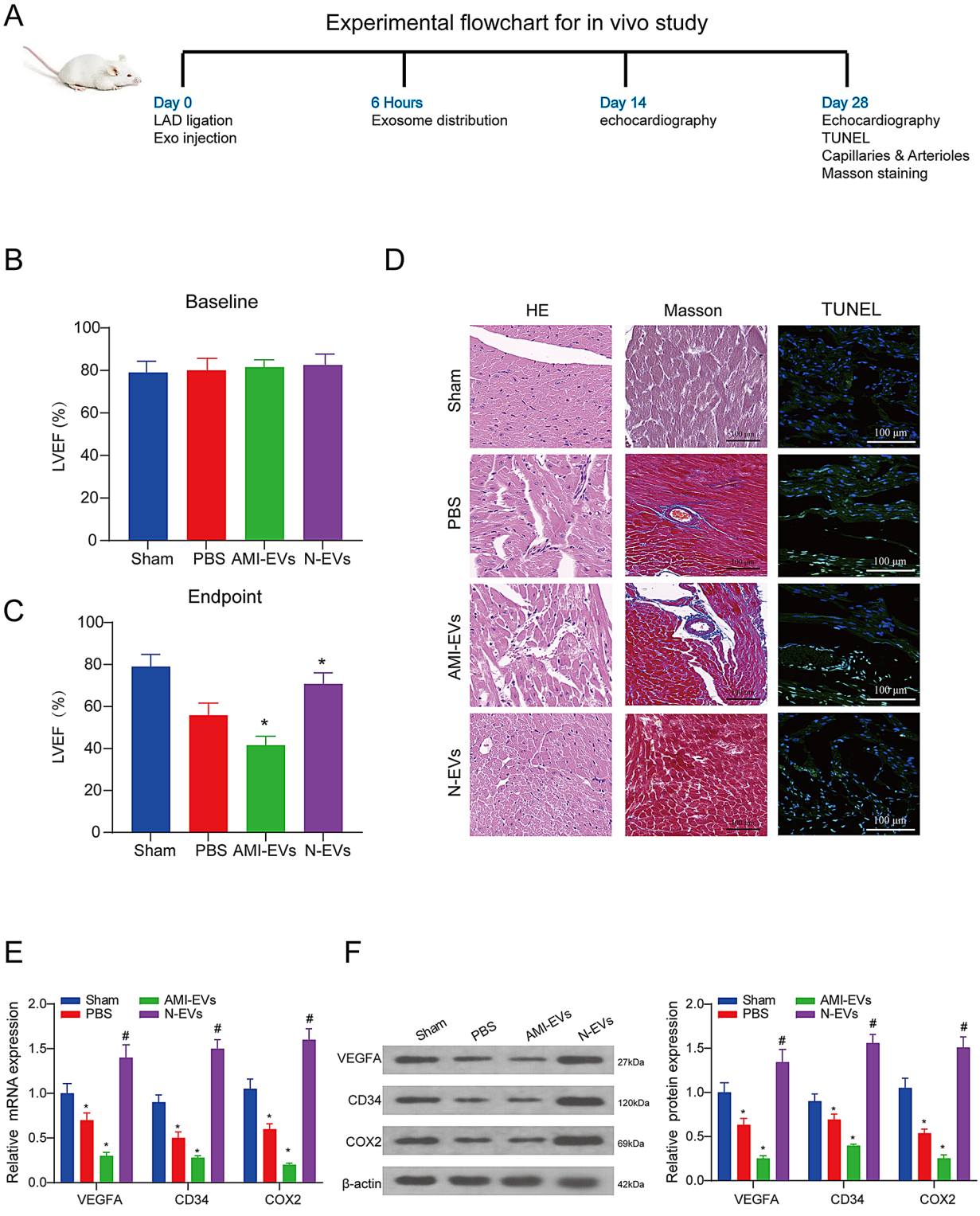

Fig. 2 (See legend on next page.)

was assessed, revealing that N-EVs significantly enhanced cell proliferation (Fig. 1B). Conversely, AMI-EVs further suppressed cell proliferation as confirmed by EdU staining and Colony formation assay (Fig. 1C-D). Moreover, examination of apoptosis in both cell types demonstrated contrasting effects; AMI-EVs notably promoted apoptosis while N-EV inhibited it (Fig. 1E). Finally, evaluation of HUVECs' migration and tube-forming capacity

(See figure on previous page.)

Fig. 2 Effects of EVs from different sources on cardiac function in a mouse model of acute myocardial infarction. (**A**) Schematic diagram of the in vivo experimental design. Legend: Schematic diagram of the in vivo experimental design. The timeline shows the key steps and time points for the myocardial infarction (MI) model, including surgery, treatment administration, and endpoint measurements. Mice were randomly divided into the control group and the treatment group. The treatment group received N-EVs (50 μg/mL) intravenously, while the control group received an equal volume of PBS. Left ventricular ejection fraction (LVEF) and left ventricular fractional shortening (LVFS) were measured at 2 weeks and 4 weeks post-MI using echocardiography. The figure illustrates the overall experimental setup and timeline. (**B**-**C**) The left ventricular ejection fraction (LVEF) was assessed using echocardiography at baseline (1 day prior to myocardial infarction) and endpoint (3 weeks after myocardial infarction). Legend: Echocardiographic assessment of left ventricular ejection fraction (LVEF) was performed at baseline (1 day before myocardial infarction) and at the endpoint (3 weeks after myocardial infarction). The LVEF values at both time points are presented as mean ± standard deviation (SD). (**D**) Myocardial tissue staining confirmed the therapeutic effects of N-EVs and AMI-EVs on hypoxia/reoxygenation injury. Legend: Myocardial tissue sections were stained with HE, Masson's trichrome and TUNEL to assess collagen deposition and fibrosis. The figure shows representative images of myocardial tissue from the control group (PBS), N-EVs treatment group, and AMI-EVs treatment group. The extent of fibrosis is quantified as the ratio of fibrotic area to total ventricular area. The therapeutic effects of N-EVs and AMI-EVs on reducing hypoxia/reoxygenation injury are evident from the reduced fibrosis in the treatment groups compared to the control group. Scale bar: 100 μm. (**E**-**F**) QRT-PCR and WB were employed to investigate the impact of circulating EVs from different sources on the expression of angiogenic markers. Legend: (**E**) Quantitative real-time PCR (QRT-PCR) was used to measure the mRNA expression levels of angiogenic markers (VEGF, Ang-1, and HIF-1α) in myocardial tissue. (**F**) Western blot (WB) analysis was performed to evaluate the protein expression levels of the same angiogenic markers. The figure shows the relative expression levels of these markers in the control group (PBS), N-EVs treatment group, and AMI-EVs treatment group. Statistical analysis revealed a significant difference (*$P < 0.05$) compared to the PBS group, as well as a significant difference (#$P < 0.05$) compared to the AMI-EVs group

revealed that N-EVs significantly augmented these functions whereas AMI-EVs hindered them (Fig. 1F-G). In summary, the study results show that EVs from healthy sources have positive effects on cell proliferation, migration, and angiogenesis, while EVs from disease states exhibit negative outcomes, not only promoting cell death but also impairing functional recovery. This outcome not only highlights the great potential of EVs in therapeutic applications but also emphasizes the critical influence of EV source on their biological effects.

Effects of EVs from different sources on cardiac function in a mouse model of acute myocardial infarction

We induced AMI in rats through coronary ligation, followed by intramyocardial injection of AMI-EVs, N-EVs, or PBS into the MI border zone (Fig. 2A). Left ventricular ejection fraction (LVEF) was utilized to evaluate cardiac function enhancement or maintenance. There were no significant differences in LVEF among the four treatment groups at baseline (Fig. 2B). Over the subsequent three weeks, the control group exhibited a gradual decrease in LVEF, while hearts injected with N-EVs demonstrated higher LVEF compared to those of the Sham or PBS groups. Conversely, AMI-EVs-treated hearts displayed worsened LVEF when compared to PBS-treated control hearts (Fig. 2C). Through HE Masson trichrome staining and TUNEL, we observed a significant reduction in myocardial fibrosis in the N-EVs treated group. This suggests that N-EVs have potential anti-fibrotic effects, possibly by inhibiting the activation of fibroblasts and excessive deposition of collagen, thereby protecting the myocardium. In contrast, the myocardial fibrosis was significantly increased in the AMI-EVs treated group. This may be because AMI-EVs carry pro-inflammatory factors and pro-fibrotic molecules, which are released following myocardial injury and further exacerbate the fibrotic process. The different effects of N-EVs and AMI-EVs may be related to the miRNAs and protein profiles they carry. N-EVs may be enriched in anti-inflammatory and repair-related miRNAs, while AMI-EVs may be enriched in pro-inflammatory and pro-fibrotic miRNAs. (Fig. 2D). Furthermore, based on our in vitro assays indicating that EVs from different sources could regulate angiogenesis, we assessed the expression of angiogenesis markers (VEGFA, CD34 and COX2) in myocardial tissue. Compared to the Sham and PBS groups, N-EVs treatment promoted angiogenesis while AMI-EVs inhibited their expression levels (Fig. 2E-F).

EVs confer protection against oxidative stress on cardiomyocytes and endothelial cells

EVs play a crucial role in facilitating the exchange of materials and information between cells. To further validate the potential of EVs in mitigating H_2O_2-induced oxidative stress injury, HUVECs and AC16 (600 μmol/L) were subjected to H_2O_2 treatment and co-cultured with N-EVs. In CCK8 and EdU assays, N-EVs (100 μg/mL) exhibited protective effects on both HUVEC and AC16 against H_2O_2 after 24 h (Fig. 3A-B). The cytoprotective effect of N-EVs against H_2O_2-induced injury was also confirmed through apoptosis assay (Fig. 3C). Moreover, in the tube formation assay, the total branch length observed for N-EVs-treated HUVECs surpassed that of PBS- or H_2O_2-treated counterparts, indicating that N-EVs effectively safeguard cardiomyocytes and endothelial cells from H_2O_2-induced injury (Fig. 3D-E). These findings demonstrate that N-EVs have a protective effect against H_2O_2-induced oxidative stress injury, enhancing cell viability, proliferation, and angiogenic capacity in both HUVECs and AC16 cells.

The role of miR-133a-3p in EVs

The current study highlights the critical role of miRNAs in the regulatory mechanisms of EVs. Utilizing

microarray analysis, we identified a total of 10 miRNAs that were up-regulated in N-EVs, alongside a significant down-regulation of 21 miRNAs (Fig. 4A-B). Among these, we selected the three most significantly up-regulated miRNAs—miR-133a-3p, miR-144-3p, and miR-23b-3p—for validation through quantitative real-time PCR (qRT-PCR). Our findings confirmed a substantial increase in the expression of miR-133a-3p, indicating its potential as a key regulatory molecule in the N-EV-mediated proliferation of cardiomyocytes and endothelial cells (Fig. 4C).

It is acknowledged that the source of EVs (from normal individuals or AMI patients) is only one of several factors that can influence their biological effects. To better understand the broader implications, we conducted additional experiments considering patient-specific factors, including age, sex, and comorbidities. These analyses revealed that such variables do indeed modulate the effects of EVs. For instance, AMI-EVs derived from older patients exhibited even lower levels of miR-133a-3p, which correlated with a more pronounced inhibition of cell proliferation (Supplementary Fig. 2A-B). Subgroup analyses were performed to explore the differential effects of N-EVs and AMI-EVs across various patient populations. The results indicated that N-EVs from younger patients and those without comorbidities contained higher levels of miR-133a-3p, leading to a more robust promotion of cell proliferation (Supplementary Fig. 2A-B). We extended our investigation to encompass a more detailed examination of other significantly up-regulated and down-regulated miRNAs. Additional functional assays were conducted to evaluate their roles in cell proliferation and other pertinent biological processes, further supporting the importance of miR-133a-3p (Supplementary Fig. 3A-B).

To delve deeper into the role of miR-133a-3p in the EV-induced promotion of cardiomyocyte and endothelial cell proliferation, AC16 and HUVEC cells were treated with PBS, N-EVs, or AMI-EVs. qRT-PCR analysis revealed a marked upregulation of miR-133a-3p expression specifically in the N-EV-treated group, with no significant changes observed in cells treated with PBS or AMI-EVs (Fig. 4D). Notably, to rule out any potential interference from residual RNA within EV extracts, we subjected the extracts to RNase A treatment. This treatment did not alter the expression levels of miR-133a-3p (Fig. 4E), confirming its stability and specificity. Furthermore, we disrupted EVs using Triton X-100 and then treated them with RNase A to degrade the RNA encapsulated within the EVs. The results showed that the elevated expression level of miR-133a-3p observed in the N-EV-treated group was reversed (Fig. 4E), indicating that miR-133a-3p is indeed encapsulated within the EVs. Importantly, a time-dependent and dose-dependent increase in miR-133a-3p expression was observed in recipient AC16 and HUVEC cells exposed to N-EVs (Fig. 4F). This finding provides strong evidence for the encapsulation and transfer of miR-133a-3p from donor to recipient cells via EVs, underscoring its role in mediating the proliferative effects of N-EVs.

miR-133a-3p influences the PANoptosis in endothelial cells and cardiomyocytes

We have observed differential expression of miR-133a-3p in N-EVs. Additionally, to confirm the regulatory impact of miR-133a-3p on endothelial cells and cardiomyocytes, we conducted co-treatments using an inhibitor for miR-133a-3p and N-EVs. The outcomes from CCK8 and EdU assays revealed a significant reversal of the proliferative effect induced by N-EVs when inhibiting the expression of miR-133a-3p (Fig. 5A-B).

To further investigate the regulatory effect of miR-133a-3p on cell, we tested the levels of apoptosis, pyroptosis, and necroptosis in the cells. Our findings revealed a significant rise in their expression levels within EVs when miR-133a-3p was inhibited, indicating a reversal of the observed effect (Fig. 5C-F). To further investigate the type of cell death programs that occurred, we used multiple inhibitors of common cell death pathways, including apoptosis, necroptosis, ferroptosis, pyroptosis, and autophagy, to rescue the cell death induced by the combination of N-EVs and miR-133a-3p inhibitor treatment. Notably, the apoptosis inhibitor Z-VAD-FMK, the necroptosis inhibitor necrostatin-1, the ferroptosis inhibitor ferrostatin-1, and the pyroptosis inhibitor Ac-DMPD/DMLD-CMK (which inhibits gasdermin E, GSDME) all reversed the reduced cell viability and enhanced cell cytotoxicity caused by the combination of N-EVs and miR-133a-3p inhibitor treatment. However, the autophagy inhibitor 3-methyladenine and the pyroptosis inhibitor disulfiram, which blocks gasdermin D (GSDMD), did not achieve similar effects (Fig. 5G-H). None of the inhibitors resulted in complete recovery of cell viability to the levels observed in the control group (Fig. 5G-H). Therefore, we hypothesized that the combination of N-EVs and miR-133a-3p inhibitor treatment simultaneously triggers multiple forms of cell death (PANoptosis), further confirming that the observed cell death is associated with other forms of cell death, such as pyroptosis or necroptosis. Furthermore, our in vivo assays also confirmed that N-EVs could inhibit the level of PANoptosis in myocardial tissue (Supplementary Fig. 4).

MiR-133a-3p regulates PANoptosis by targeting ELAVL1

Several studies have demonstrated the crucial involvement of ELAVL1 in the regulation of PANoptosis. Using the starBase database, we identified a targeted regulatory

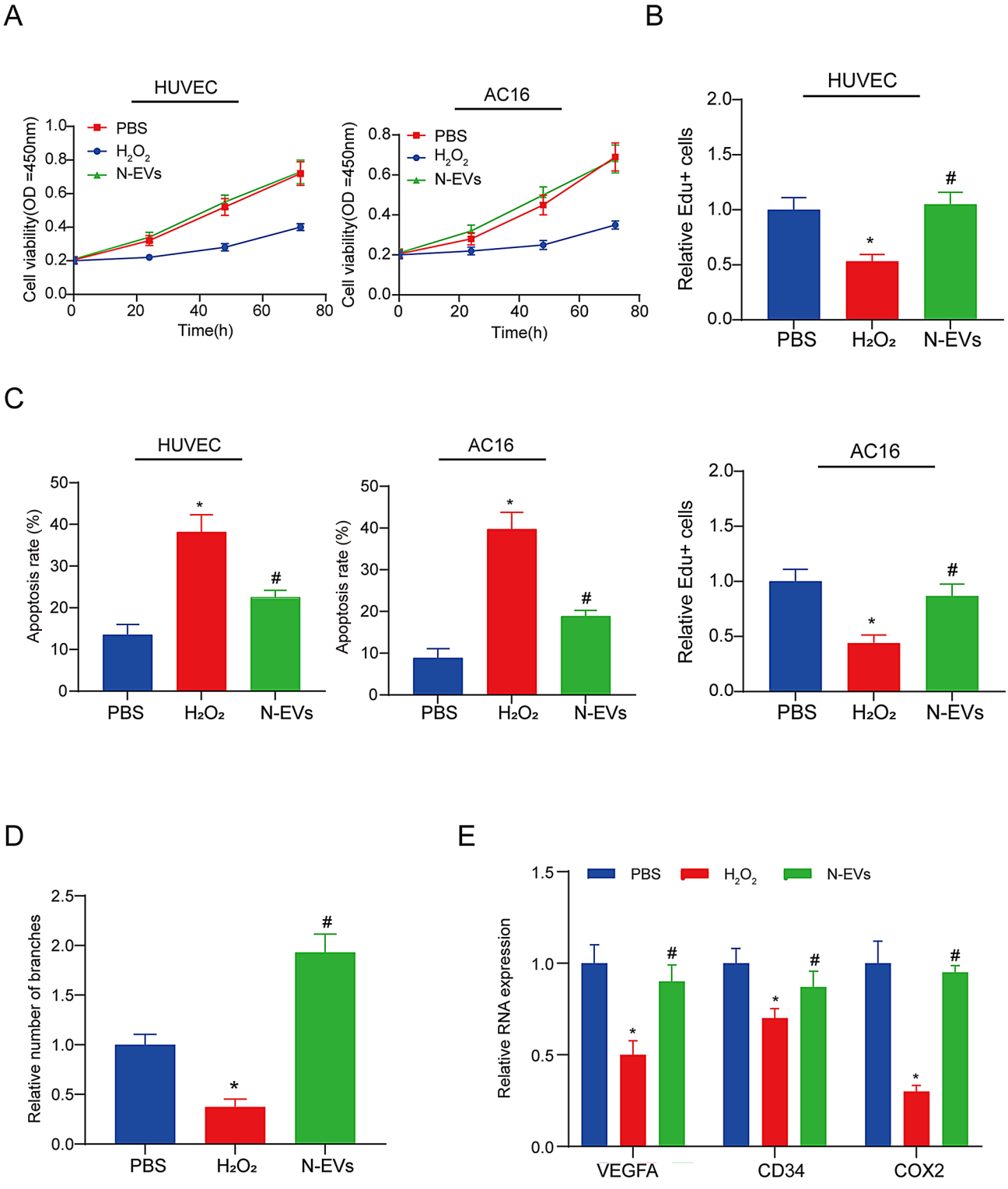

Fig. 3 (See legend on next page.)

relationship between miR-133a-3p and ELAVL1. To further explore this regulatory interplay, we conducted a series of experiments. We confirmed the specific binding of miR-133a-3p to ELAVL1 using dual-luciferase reporter and RNA immunoprecipitation (RIP) assays (Fig. 6A-B, Supplementary Fig. 5). These assays demonstrated that miR-133a-3p directly targets the 3' UTR of ELAVL1. We validated the regulatory effect of miR-133a-3p on

(See figure on previous page.)

Fig. 3 Improvement effect of N-EVs on AC16 and HUVEC after H_2O_2 treatment. (**A**) The cell proliferation ability of N-EVs on HUVEC and AC16 cells after H_2O_2 treatment was assessed using CCK8 assay. Legend: The CCK8 assay was used to evaluate the impact of normal extracellular vesicles (N-EVs) on the proliferation of HUVEC and AC16 cells after H_2O_2-induced oxidative stress. HUVEC and AC16 cells were pretreated with N-EVs (50 μg/mL) for 24 h, followed by exposure to H_2O_2 (200 μM) for another 24 h. Cell viability was assessed by measuring the absorbance at 450 nm. The figure shows the relative cell viability of HUVEC and AC16 cells in the following groups: control (no treatment), H_2O_2 treatment alone, and H_2O_2 treatment with N-EVs. (**B**) EdU assay was employed to evaluate the cell proliferation ability of EVs on HUVEC and AC16 cells after H_2O_2 treatment. Legend: The EdU (5-ethynyl-2'-deoxyuridine) assay was used to assess the impact of N-EVs on the proliferation of HUVEC and AC16 cells after H_2O_2-induced oxidative stress. HUVEC and AC16 cells were pretreated with N-EVs (50 μg/mL) for 24 h, followed by exposure to H_2O_2 (200 μM) for another 24 h. EdU incorporation into newly synthesized DNA was detected using a fluorescence microscope. The figure shows the percentage of EdU-positive cells in the following groups: control (no treatment), H_2O_2 treatment alone, and H_2O_2 treatment with N-EVs. (**C**) Flow cytometry analysis was conducted to determine the apoptosis rate in different treatment groups. Legend: Flow cytometry was used to analyze the apoptosis rate in HUVEC and AC16 cells after H_2O_2-induced oxidative stress and treatment with N-EVs. Cells were pretreated with N-EVs (50 μg/mL) for 24 h, followed by exposure to H_2O_2 (200 μM) for another 24 h. Apoptosis was detected using Annexin V-FITC/PI double staining. The figure shows the proportions of early apoptotic (Annexin V + PI-), late apoptotic (Annexin V + PI+), and necrotic cells (Annexin V- PI+) in the following groups: control (no treatment), H_2O_2 treatment alone, and H_2O_2 treatment with N-EVs. (**D**) Angiogenesis assays were performed to assess the impact of N-EVs on tube formation capability. Legend: Angiogenesis assays were conducted to evaluate the impact of N-EVs on the tube formation capability of HUVEC cells. HUVEC cells were seeded on Matrigel and treated with N-EVs (50 μg/mL) for 6 h. Tube formation was observed and photographed under a phase-contrast microscope. The figure shows representative images of tube formation and quantification of the total tube length and number of branch points in the following groups: control (no treatment), H_2O_2 treatment alone, and H_2O_2 treatment with N-EVs. (**E**) QRT-PCR analysis was utilized to examine the effects of different treatments on the expression levels of angiogenic markers. Legend: Quantitative real-time PCR (QRT-PCR) was used to examine the effects of N-EVs on the mRNA expression levels of angiogenic markers (VEGF, Ang-1, and HIF-1α) in HUVEC and AC16 cells after H_2O_2-induced oxidative stress. HUVEC and AC16 cells were pretreated with N-EVs (50 μg/mL) for 24 h, followed by exposure to H_2O_2 (200 μM) for another 24 h. The figure shows the relative mRNA expression levels of VEGF, Ang-1, and HIF-1α in the following groups: control (no treatment), H_2O_2 treatment alone, and H_2O_2 treatment with N-EVs. Statistical significance was determined by comparing with PBS group (*$P < 0.05$), as well as H_2O_2 group (#$P < 0.05$)

cardiomyocyte proliferation using CCK8 and apoptosis assays. The results showed that ELAVL1 acts as a target gene of miR-133a-3p, with miR-133a-3p overexpression leading to increased cell proliferation and reduced apoptosis (Fig. 6C-D). We assessed markers of PANoptosis and found that miR-133a-3p exerts its regulatory role by modulating the expression of ELAVL1. Specifically, overexpression of miR-133a-3p led to a decrease in the expression of PANoptosis markers, while knockdown of miR-133a-3p resulted in increased expression of these markers (Fig. 6E-F). These findings provide strong evidence that miR-133a-3p regulates PANoptosis by targeting ELAVL1, highlighting the importance of this miRNA in the modulation of cell death pathways. Meanwhile, we tested the expression of ELAVL1 and pan-apoptotic protein by in vivo experiments to further verify the mechanism by which miR-133a-3p regulates cardiac injury in vivo. The results showed that ELAVL1-positive stained capillaries in the border zone 4 weeks post-MI. Immunofluorescence staining shows ELAVL1-positive capillaries in the left ventricular border zone. Immunofluorescence staining showed a lower density of ELAVL1-positive capillaries in the border zone of N-EV-treated rats compared to the PBS group, indicating improved angiogenesis (Supplementary Fig. 6A). Western blot analysis of PANoptosis-related protein expression. Proteins detected include cleaved caspase-3 (apoptosis marker), cleaved caspase-1 (pyroptosis marker), GSDMD (pyroptosis marker), MLKL (necroptosis marker), and RIPK3 (necroptosis marker). β-actin was used as the loading control. Western blot analysis showed that N-EVs downregulated the expression of PANoptosis-related proteins, including cleaved caspase-3, cleaved caspase-1, GSDMD, MLKL, and RIPK3, in the hearts of treated rats (Supplementary Fig. 6B-D). These results collectively demonstrate that N-EVs effectively preserved cardiac function, reduced fibrosis, promoted angiogenesis, and inhibited PANoptosis in rats with myocardial infarction.

ELAVL1 influences the formation of the PANoptosome by affecting the stability of NLRP3 mRNA

To delve deeper into the mechanism by which ELAVL1 regulates PANoptosis, we first established ELAVL1 as an RNA-binding protein (RBP). Using predictions from the starBase database, we identified ELAVL1 as an RBP that specifically interacts with NLRP3 mRNA (Fig. 7A). Upon knocking down ELAVL1, we observed no significant changes in the mRNA expression levels of NLRP3 (Fig. 7B), but there was a marked effect on the protein expression of NLRP3 (Fig. 7C). This led us to hypothesize that ELAVL1 influences the protein expression of NLRP3 by affecting the stability of its mRNA. Our experiments confirmed this hypothesis (Fig. 7D). Subsequently, we used the ATtRACT database to predict three binding sites for ELAVL1 on NLRP3 mRNA (Fig. 7E). Through luciferase reporter assays, we validated these predicted sites and identified site P1 as the critical binding region through which ELAVL1 exerts control over NLRP3 (Fig. 7F-G). Additionally, RNA immunoprecipitation (RIP) assays provided concrete evidence of the physical interaction between ELAVL1 protein and NLRP3 mRNA (Fig. 7H). Collectively, these findings demonstrate that ELAVL1 regulates PANoptosis by modulating the stability of NLRP3 mRNA (Fig. 7I).

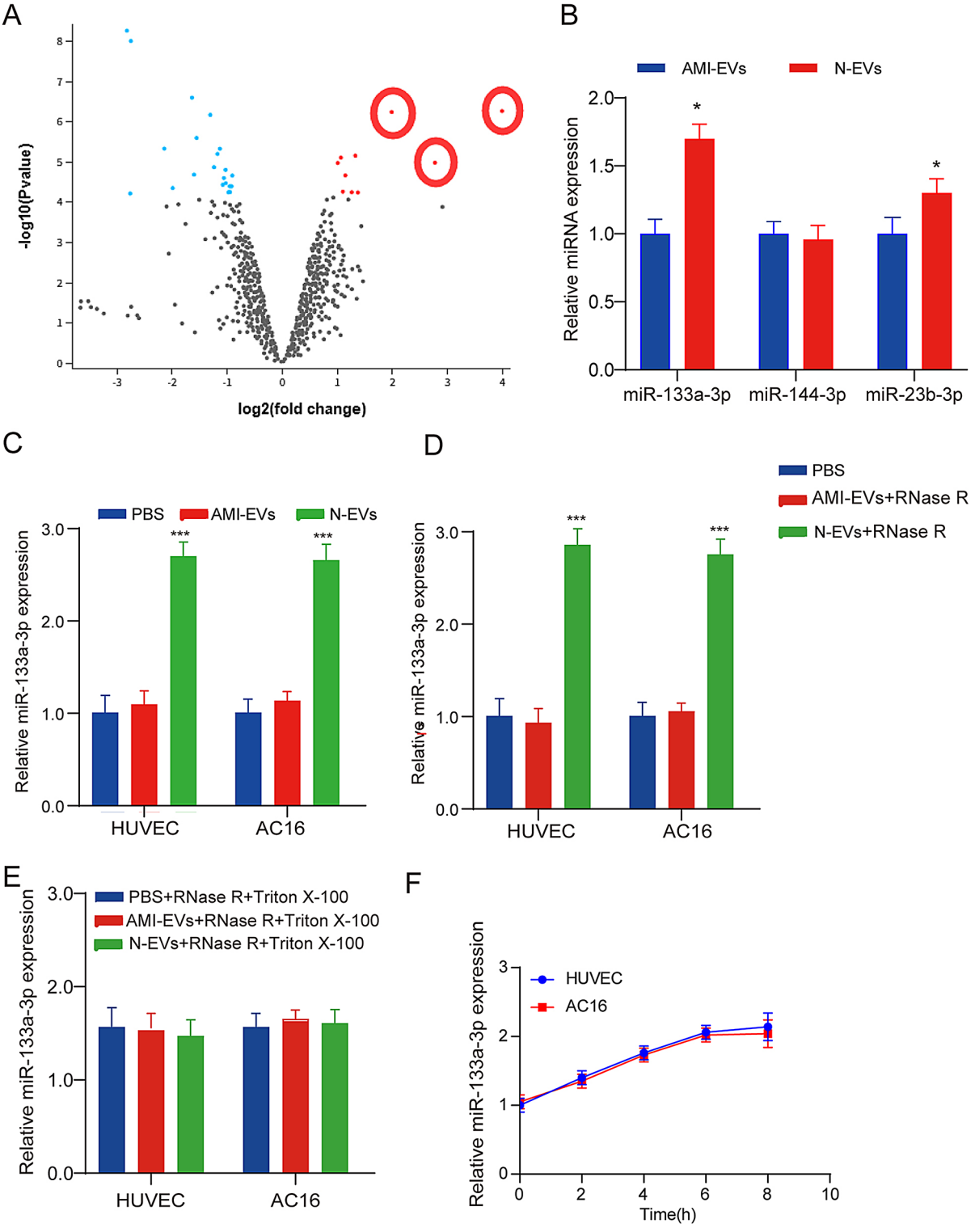

Fig. 4 (See legend on next page.)

Discussion

In this study, we initially investigated the impact of circulating EVs derived from various sources on myocardial injury and discovered that N-EVs exhibited therapeutic potential in treating ischemia/reperfusion-induced myocardial injury. Furthermore, we confirmed the protective effects of N-EVs against hydrogen peroxide-induced cardiomyocyte and endothelial cell injury, as well as

(See figure on previous page.)

Fig. 4 The role of miR-133a-3p in EVs. (**A**) Volcano plots were employed to visualize differentially expressed miRNAs in the two types of circulating EVs. Legend: Volcano plots were generated to visualize the differentially expressed miRNAs in circulating EVs derived from normal (N-EVs) and acute myocardial infarction (AMI-EVs) samples. Each dot represents a specific miRNA, with the x-axis showing the log2 fold change (log2FC) and the y-axis showing the -log10 p-value. Red dots indicate significantly upregulated miRNAs, blue dots indicate significantly downregulated miRNAs, and gray dots represent non-significantly changed miRNAs. The figure highlights key miRNAs, including miR-133a-3p, miR-144-3p, and miR-23b-3p, which show differential expression between N-EVs and AMI-EVs. Data were normalized and analyzed using DESeq2. (**B**) The expression levels of miR-133a-3p, miR-144-3p, and miR-23b-3p in EVs derived from various sources were quantified using QRT-PCR. Legend: Quantitative real-time PCR (QRT-PCR) was used to quantify the expression levels of miR-133a-3p, miR-144-3p, and miR-23b-3p in EVs derived from different sources, including normal (N-EVs) and acute myocardial infarction (AMI-EVs) samples. The figure shows the relative expression levels of these miRNAs, normalized to U6 snRNA. (**C**) The abundance of miR-133a-3p was assessed after treatment with AMI-EV or N-EV at a concentration of 5 μg/mL. Legend: The abundance of miR-133a-3p was measured in HUVEC and AC16 cells after treatment with AMI-EVs or N-EVs at a concentration of 5 μg/mL for 24 h. QRT-PCR was used to quantify the miR-133a-3p levels, normalized to U6 snRNA. The figure shows the relative expression levels of miR-133a-3p in the control (no EV treatment), N-EV treatment, and AMI-EV treatment groups. (**D**) The level of miR-133a-3p expression was determined in RNase A-treated EVs (0.1 mg/mL). Legend: The stability of miR-133a-3p in EVs was assessed by treating EVs with RNase A (0.1 mg/mL) for 30 min at 37 °C. QRT-PCR was used to quantify the miR-133a-3p levels in RNase A-treated and untreated EVs, normalized to U6 snRNA. The figure shows the relative expression levels of miR-133a-3p in the control (untreated EVs) and RNase A-treated EVs. (**E**) QRT-PCR analysis was performed to evaluate the presence of miR-133a-3p in Triton X-100-treated (0.3%) and RNase-digested EVs. Legend: The integrity and protection of miR-133a-3p within EVs were evaluated by treating EVs with Triton X-100 (0.3%) and RNase A (0.1 mg/mL). QRT-PCR was used to quantify the miR-133a-3p levels in the following groups: control (untreated EVs), Triton X-100-treated EVs, and RNase A-digested EVs, normalized to U6 snRNA. The figure shows the relative expression levels of miR-133a-3p in each group. (**F**) The impact of EV treatment dose on the expression level of miR-133a-3p in AC16 and HUVEC cells was investigated through time-dependent and dose-replacement experiments. Legend: Time-dependent and dose-replacement experiments were conducted to investigate the impact of EV treatment on the expression level of miR-133a-3p in AC16 and HUVEC cells. HUVEC and AC16 cells were treated with N-EVs or AMI-EVs at different concentrations (1, 5, and 10 μg/mL) for various time points (24, 48, and 72 h). QRT-PCR was used to quantify the miR-133a-3p levels, normalized to U6 snRNA. The figure shows the relative expression levels of miR-133a-3p in the following groups: control (no EV treatment), N-EV treatment, and AMI-EV treatment at different doses and time points. Statistical significance was determined by comparing with AMI-EVs group (*$P < 0.05$)

their ability to promote cardiomyocyte proliferation and angiogenesis. These findings partially elucidate the underlying mechanisms responsible for the therapeutic efficacy of N-EVs in myocardial injury. Lastly, through microarray analysis, we identified that N-EVs could suppress cardiomyocyte PANoptosis by targeting ELAVL1 via delivery of miR-133a-3p. N-EVs exert their protective effects by delivering miR-133a-3p, which targets ELAVL1 and inhibits its expression. High expression of ELAVL1 enhances the stability of NLRP3 mRNA, leading to increased NLRP3 protein expression. Elevated NLRP3 expression promotes the formation of the PANoptosome, triggering PANoptosis and ultimately contributing to acute myocardial infarction (AMI). By delivering miR-133a-3p, N-EVs can inhibit this process, thereby improving AMI outcomes. These novel insights provide valuable directions for developing innovative treatments for myocardial injury.

Previous studies have found that circulating EVs play different regulatory roles on cardiomyocyte injury [13]. Recent data demonstrate that exosomes engage in cellular interactions through diverse mechanisms, encompassing (a) ligand-receptor binding-mediated recognition of surface receptors on target cells by exosomes, thereby initiating signal transduction; (b) direct fusion between exosomes and target cells to facilitate intercellular receptor transfer and subsequent signal transduction; (c) fusion of exosomes with target cells leading to the release of internal proteins into the cytoplasm of recipient cells, thereby exerting biological functions; (d) delivery of genetic information to target cells by exosomes via mRNA, microRNAs or other transcription factors [13, 14, 15]. Our study shows that circulating exosomes can be taken up by cells and undertake intercellular communication while maintaining membrane structure and internal substances, these data support a possible mechanism for the protective effect of circulating EVs against myocardial injury.

Multiple studies have demonstrated the ability of EVs to encapsulate and transport miRNAs into cells, thereby facilitating their functional roles. The differential expression of miRNAs within EVs compared to blood underscores the significance of investigating these molecules in EVs. Therefore, this study aimed to employ microarray analysis as a starting point for identifying the distinct expression pattern of miR-133a-3p in circulating EVs derived from various sources, with subsequent experiments validating this discovery. As a specific miRNA, the investigation of miR-133a-3p in exosomes is still in its preliminary stage; however, its potential as a biomarker and intercellular communication mediator has garnered significant attention [1, 16]. Particularly in the realm of myocardial injury, miR-133a-3p has demonstrated anti-apoptotic effects and holds promise as a diagnostic biomarker for myocardial injury while being involved in mechanisms related to myocardial protection. These findings offer novel perspectives and potential targets for further research and treatment of cardiac diseases. Our findings indicate that N-EVs possess the ability to modulate cardiomyocyte proliferation and endothelial cell angiogenesis through the action of miR-133a-3p [17, 18, 19].

PANoptosis, an essential form of cell death during MI/R injury, is accompanied by the release of numerous

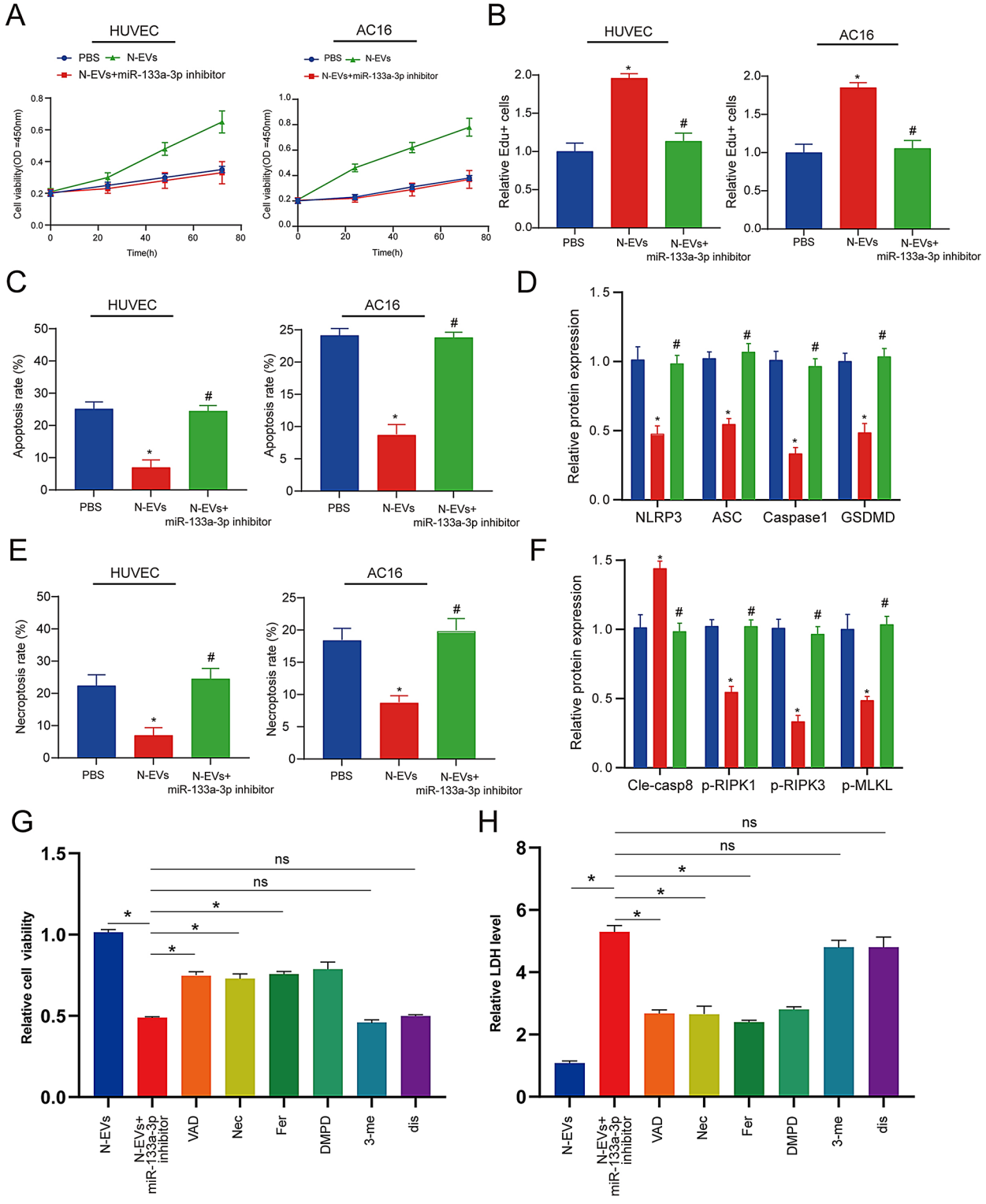

Fig. 5 (See legend on next page.)

inflammatory factors which contribute to further damage in surrounding tissues [20, 21]. As a pivotal RNA-binding protein, ELAVL1 (also known as HuR) has garnered increasing attention in the field of PANoptosis research. Studies have demonstrated that ELAVL1 exerts regulatory control over the expression of key PANoptosis-related proteins such as caspase-1 and NLRP3, thereby actively participating in the signaling pathway governing

(See figure on previous page.)

Fig. 5 The impact of miR-133a-3p on endothelial cells and cardiomyocytes. (**A**) The cell proliferation ability of N-EVs and miR-133a-3p inhibitor on HUVEC and AC16 was assessed using the CCK8 assay. Legend: The CCK8 assay was used to evaluate the impact of N-EVs and the miR-133a-3p inhibitor on the proliferation of HUVEC and AC16 cells. Cells were treated with N-EVs (50 μg/mL) alone, the miR-133a-3p inhibitor (100nM) alone, or a combination of both for 24 h. Cell viability was assessed by measuring the absorbance at 450 nm. The figure shows the relative cell viability of HUVEC and AC16 cells in the following groups: control (no treatment), N-EVs treatment, miR-133a-3p inhibitor treatment, and combined treatment. (**B**) The cell proliferation ability of N-EVs and miR-133a-3p inhibitor on HUVEC and AC16 was evaluated by EdU staining. Legend: The EdU (5-ethynyl-2′-deoxyuridine) staining assay was used to assess the impact of N-EVs and the miR-133a-3p inhibitor on the proliferation of HUVEC and AC16 cells. Cells were treated with N-EVs (50 μg/mL) alone, the miR-133a-3p inhibitor (100 nM) alone, or a combination of both for 24 h. EdU incorporation into newly synthesized DNA was detected using a fluorescence microscope. The figure shows the percentage of EdU-positive cells in the following groups: control (no treatment), N-EVs treatment, miR-133a-3p inhibitor treatment, and combined treatment. (**C**, **E**) Flow cytometry was employed to determine the apoptosis rate and necroptosis rate in different treatment groups. Legend: (**C**) Flow cytometry was used to analyze the apoptosis rate in HUVEC and AC16 cells after treatment with N-EVs (50 μg/mL) alone, the miR-133a-3p inhibitor (100nM) alone, or a combination of both for 24 h. Apoptosis was detected using Annexin V-FITC/PI double staining. The figure shows the proportions of early apoptotic (Annexin V + PI-), late apoptotic (Annexin V + PI+), and necrotic cells (Annexin V- PI+) in the following groups: control (no treatment), N-EVs treatment, miR-133a-3p inhibitor treatment, and combined treatment. Legend: (**E**) Flow cytometry was used to analyze the necroptosis rate in HUVEC and AC16 cells after treatment with N-EVs (50 μg/mL) alone, the miR-133a-3p inhibitor (100nM) alone, or a combination of both for 24 h. Necroptosis was detected using a specific necroptosis marker (e.g., MLKL phosphorylation). The figure shows the proportions of necroptotic cells in the following groups: control (no treatment), N-EVs treatment, miR-133a-3p inhibitor treatment, and combined treatment. (**D**, **F**) Western Blot analysis was conducted to examine the effects of different treatments on the expression of pyroptosis and necroptosis markers. Legend: (**D**) Western blot analysis was used to examine the effects of N-EVs and the miR-133a-3p inhibitor on the expression of pyroptosis markers (e.g., cleaved caspase-1, GSDMD) in HUVEC and AC16 cells. Cells were treated with N-EVs (50 μg/mL) alone, the miR-133a-3p inhibitor (100nM) alone, or a combination of both for 24 h. The figure shows the protein expression levels of cleaved caspase-1 and GSDMD in the following groups: control (no treatment), N-EVs treatment, miR-133a-3p inhibitor treatment, and combined treatment. Legend: (**F**) Western blot analysis was used to examine the effects of N-EVs and the miR-133a-3p inhibitor on the expression of necroptosis markers (e.g., phosphorylated MLKL, RIPK3) in HUVEC and AC16 cells. Cells were treated with N-EVs (50 μg/mL) alone, the miR-133a-3p inhibitor (100nM) alone, or a combination of both for 24 h. The figure shows the protein expression levels of phosphorylated MLKL and RIPK3 in the following groups: control (no treatment), N-EVs treatment, miR-133a-3p inhibitor treatment, and combined treatment. (**G**-**H**) Cell Viability (**G**) and Cytotoxicity (**H**) Assessments. Legend: (**G**) and (**H**) respectively assess the cell viability and cytotoxicity of HUVEC cells under the following conditions: treatment with N-EVs alone or in combination with a miR-133a-3p inhibitor for 24 h, along with the addition of the apoptosis inhibitor Z-VAD-FMK (VAD, 25 μM), the necroptosis inhibitor necrostatin (Nec, 20 μM), the ferroptosis inhibitor ferrostatin-1 (Fer, 10 μM), the pyroptosis inhibitors Ac-DMPD/DMLD-CMK (DMPD/DMLD, 20 μM) and disulfiram (dis, 1 μM), and the autophagy inhibitor 3-methyladenine (3-me, 10 μM). Statistical significance was determined as * vs. PBS group, $P < 0.05$; # vs. N-EVs group, $P < 0.05$

pyroptotic processes and exerting profound influence on their initiation and progression [22, 23]. Notably, alterations in ELAVL1 expression have been observed to exhibit a direct correlation with augmented or diminished levels of PANoptosis within specific disease models. Although the precise underlying mechanism by which ELAVL1 modulates PANoptosis remains incompletely elucidated, harnessing its potential as both a therapeutic target and strategy holds significant promise [24, 25, 26, 27]. Future investigations will delve deeper into unraveling the intricate workings of ELAVL1 within the context of PANoptosis, potentially unveiling novel applications for targeted intervention against specific diseases. The present study demonstrates that N-EVs effectively suppress the expression of ELAVL1 in MI/R cardiomyocytes, thereby attenuating PANoptosis and offering promising clinical implications for mitigating and preventing MI/R injury in ischemic cardiomyopathy.

Our study reveals that miR-133a-3p plays a crucial role in regulating PANoptosis in cardiac cells through its interaction with ELAVL1. This finding adds to the growing body of literature on the importance of miRNAs in modulating various forms of cell death, particularly in the context of cardiac diseases. While previous studies have demonstrated the role of miRNAs such as miR-29a-3p and miR-18a in regulating PANoptosis in non-cardiac tissues, our study is one of the first to specifically address this mechanism in the heart. MiR-29a-3p has been shown to reduce PANoptosis in alveolar epithelial cells, thereby improving acute lung injury [28]. This effect is mediated through the downregulation of pro-inflammatory cytokines and the promotion of cell survival. In contrast, our study demonstrates that miR-133a-3p interacts with ELAVL1 to specifically modulate PANoptosis in cardiac cells. This highlights the tissue-specific nature of miRNA functions and suggests that the mechanisms underlying PANoptosis regulation may vary significantly across different organ systems. MiR-18a regulates tumor necrosis factor-α (TNF-α)-induced PANoptosis in osteoblasts through hypoxia-inducible factor-1α (HIF-1α) [29]. This pathway is crucial for maintaining bone homeostasis under hypoxic conditions. Our findings indicate that miR-133a-3p also regulates TNF-α-induced PANoptosis, but through a different mechanism involving ELAVL1. This suggests that while the ultimate goal of reducing cell death is similar, the specific pathways and interactions differ between cardiac and osteoblastic cells. The interaction between miR-133a-3p and ELAVL1 in cardiac cells is a novel and important discovery. ELAVL1, also known as HuR, is a well-characterized RNA-binding protein that stabilizes mRNAs and enhances their translation. By targeting ELAVL1, miR-133a-3p likely affects the stability and translation of mRNAs involved in PANoptosis pathways. This mechanism provides a new perspective

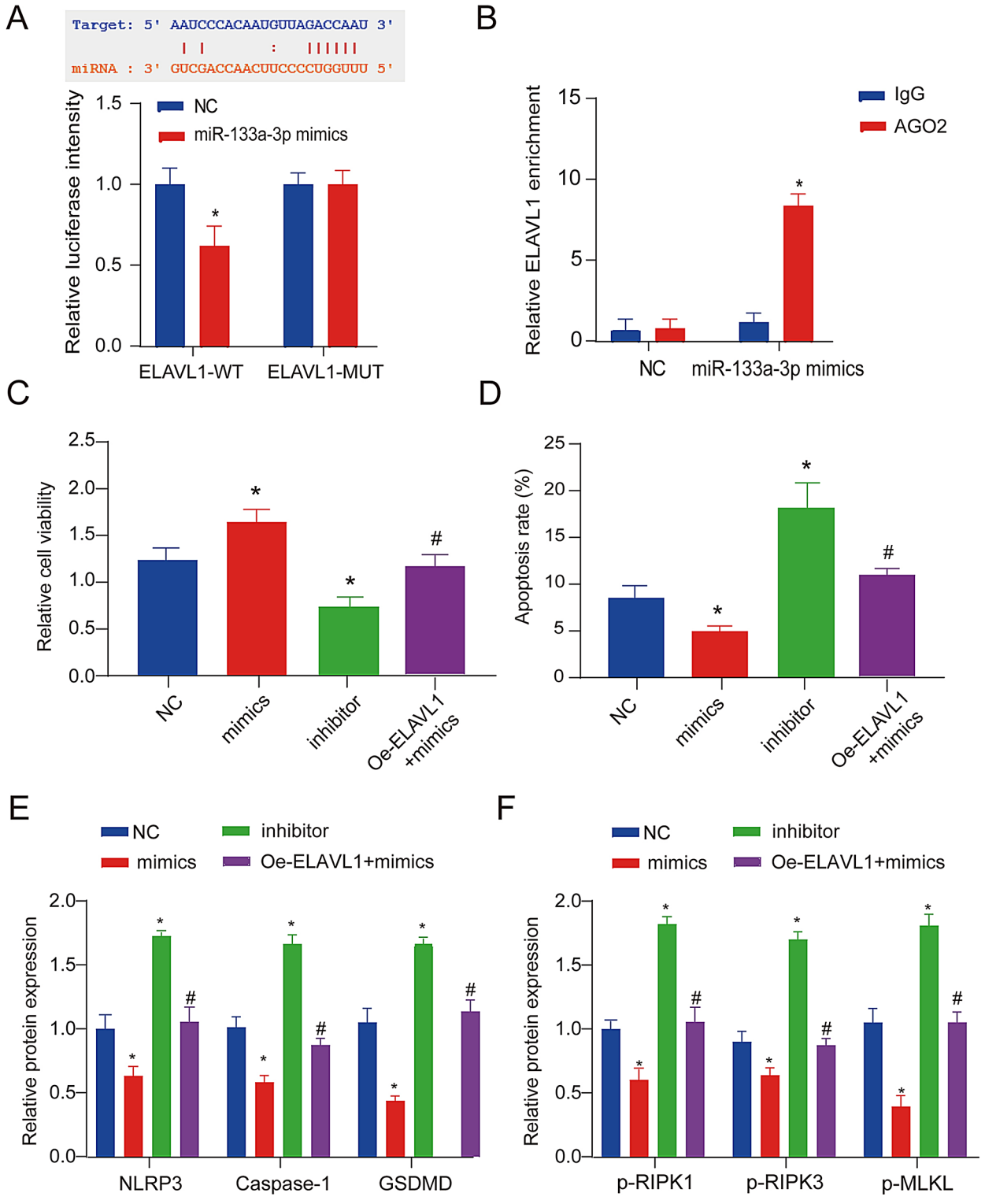

Fig. 6 (See legend on next page.)

on how miRNAs can fine-tune cellular responses to stress and injury in the heart.Studies have reported that exosomal miR-133a-3p derived from BMSCs reduces brain ischemia-reperfusion injury by targeting DAPK2 [30]. This finding indicates a neuroprotective role of miR-133a-3p. Another study showed that miR-133a-3p inhibits pyroptosis activation by targeting IKKepsilon, thereby alleviating cardiomyocyte hypertrophy [31]. This

(See figure on previous page.)

Fig. 6 MiR-133a-3p regulates PANoptosis by targeting ELAVL1. (**A**) The targeting relationship between miR-133a-3p and ELAVL1 was confirmed by the dual-luciferase reporter assay. Legend: The dual-luciferase reporter assay was used to confirm the direct targeting relationship between miR-133a-3p and ELAVL1. The 3' untranslated region (3'UTR) of ELAVL1 containing the putative miR-133a-3p binding site was cloned into a luciferase reporter vector (ELAVL1-WT). A mutant version of the 3'UTR with the binding site deleted (ELAVL1-Mut) was also constructed. HEK293T cells were co-transfected with the reporter vectors and either miR-133a-3p mimic or a negative control (NC) mimic. Luciferase activity was measured 48 h post-transfection. The figure shows the relative luciferase activity in the following groups: NC mimic + ELAVL1-WT, miR-133a-3p mimic + ELAVL1-WT, NC mimic + ELAVL1-Mut, and miR-133a-3p mimic + ELAVL1-Mut. (**B**) The mutual binding of miR-133a-3p and ELAVL1 was validated through the RIP assay. Legend: RNA immunoprecipitation (RIP) assay was performed to validate the mutual binding of miR-133a-3p and ELAVL1. HUVEC and AC16 cells were lysed, and the cell lysates were incubated with magnetic beads conjugated with anti-ELAVL1 antibody or IgG (negative control). The enriched RNA was extracted and subjected to qRT-PCR to quantify the levels of miR-133a-3p. The figure shows the relative enrichment of miR-133a-3p in the ELAVL1-bound fraction compared to the IgG control. (**C**) Cell viability in different treatment groups was assessed using CCK8. Legend: The CCK8 assay was used to assess the cell viability of HUVEC and AC16 cells in different treatment groups. Cells were treated with N-EVs (50 μg/mL), miR-133a-3p inhibitor (100 nM), or a combination of both for 24 h. Cell viability was measured by assessing the absorbance at 450 nm. The figure shows the relative cell viability in the following groups: control (no treatment), N-EVs treatment, miR-133a-3p inhibitor treatment, and combined treatment. (**D**) Flow cytometry was employed to determine the apoptosis rate in different treatment groups. Legend: Flow cytometry was used to analyze the apoptosis rate in HUVEC and AC16 cells after treatment with N-EVs (50 μg/mL), miR-133a-3p inhibitor (100nM), or a combination of both for 24 h. Apoptosis was detected using Annexin V-FITC/PI double staining. The figure shows the proportions of early apoptotic (Annexin V + PI-), late apoptotic (Annexin V + PI+), and necrotic cells (Annexin V- PI+) in the following groups: control (no treatment), N-EVs treatment, miR-133a-3p inhibitor treatment, and combined treatment. (**E**, **F**) WB were utilized to examine the expression of pyroptosis and necroptosis markers in different treatment groups. Legend: (**E**) Western blot analysis was used to examine the expression of pyroptosis markers (cleaved caspase-1 and GSDMD) in HUVEC and AC16 cells after treatment with N-EVs (50 μg/mL), miR-133a-3p inhibitor (100 nM), or a combination of both for 24 h. The figure shows the protein expression levels of cleaved caspase-1 and GSDMD in the following groups: control (no treatment), N-EVs treatment, miR-133a-3p inhibitor treatment, and combined treatment. Legend: (**F**) Western blot analysis was used to examine the expression of necroptosis markers (phosphorylated MLKL and RIPK3) in HUVEC and AC16 cells after treatment with N-EVs (50 μg/mL), miR-133a-3p inhibitor (100nM), or a combination of both for 24 h. The figure shows the protein expression levels of phosphorylated MLKL and RIPK3 in the following groups: control (no treatment), N-EVs treatment, miR-133a-3p inhibitor treatment, and combined treatment. Statistical significance was denoted as * vs. NC group ($P < 0.05$), # vs. inhibitor group ($P < 0.05$)

further supports the protective role of miR-133a-3p in cardiovascular health. Research has also demonstrated that miR-133a-3p mitigates oxidative stress-induced trophoblast apoptosis through the BACH1/Nrf2/HO-1 signaling pathway [32]. This indicates the importance of miR-133a-3p in antioxidant defense. Despite the diverse roles of miR-133a-3p in different tissues, these roles may be tissue-specific. For example, in brain tissue, miR-133a-3p functions by targeting DAPK2, while in the heart, it may regulate PANoptosis through a different pathway, such as targeting ELAVL1. This tissue specificity could explain the observed differences across studies. MiR-133a-3p may regulate multiple cell death pathways through different targets. For instance, it can influence apoptosis by targeting DAPK2, pyroptosis by targeting IKKepsilon, and PANoptosis by targeting ELAVL1. This multi-target regulation mechanism could account for the various functions of miR-133a-3p in different settings. Different experimental conditions and pathological states may affect the function of miR-133a-3p. For example, the mechanisms of action of miR-133a-3p may vary under conditions such as ischemia-reperfusion injury and oxidative stress. Therefore, future studies should validate the specific mechanisms of miR-133a-3p under a wider range of pathological conditions. Future research should systematically investigate the multi-target regulation mechanisms of miR-133a-3p in different tissues and pathological conditions to gain a more comprehensive understanding of its functions. Based on the current findings, exploring the clinical translation potential of miR-133a-3p in cardiac diseases, particularly in the regulation of PANoptosis, will be an important direction for future research. By adding these points, we aim to provide a more comprehensive consideration of potential contradictions and alternative explanations, thereby strengthening our arguments. Thank you again for your valuable feedback, and we look forward to your further guidance.

Specifically, our study demonstrates that miR-133a-3p, delivered by N-EVs, binds to the 3' UTR of ELAVL1, reducing its expression. ELAVL1, as an RNA-binding protein, stabilizes NLRP3 mRNA, thereby increasing NLRP3 protein levels. High NLRP3 expression facilitates the formation of the PANoptosome, a key step in PANoptosis. The formation of the PANoptosome not only leads to cell death but also triggers inflammatory responses, exacerbating myocardial damage. By delivering miR-133a-3p, N-EVs effectively inhibit ELAVL1 expression, which in turn reduces the stability of NLRP3 mRNA and decreases NLRP3 protein levels. This mechanism prevents the formation of the PANoptosome and reduces the occurrence of PANoptosis, thereby mitigating the pathological progression of AMI. Our experimental results show that N-EVs treatment significantly improves cardiac function, reduces fibrosis, promotes angiogenesis, and decreases cell apoptosis in rats with myocardial infarction.

Although our study is the first to demonstrate the therapeutic potential of N-EVs in myocardial injury, further investigation revealed the crucial role of miR-133a-3p/ELAVL1 pathway in regulating cardiomyocyte PANoptosis. However, due to insufficient clinical research data, it

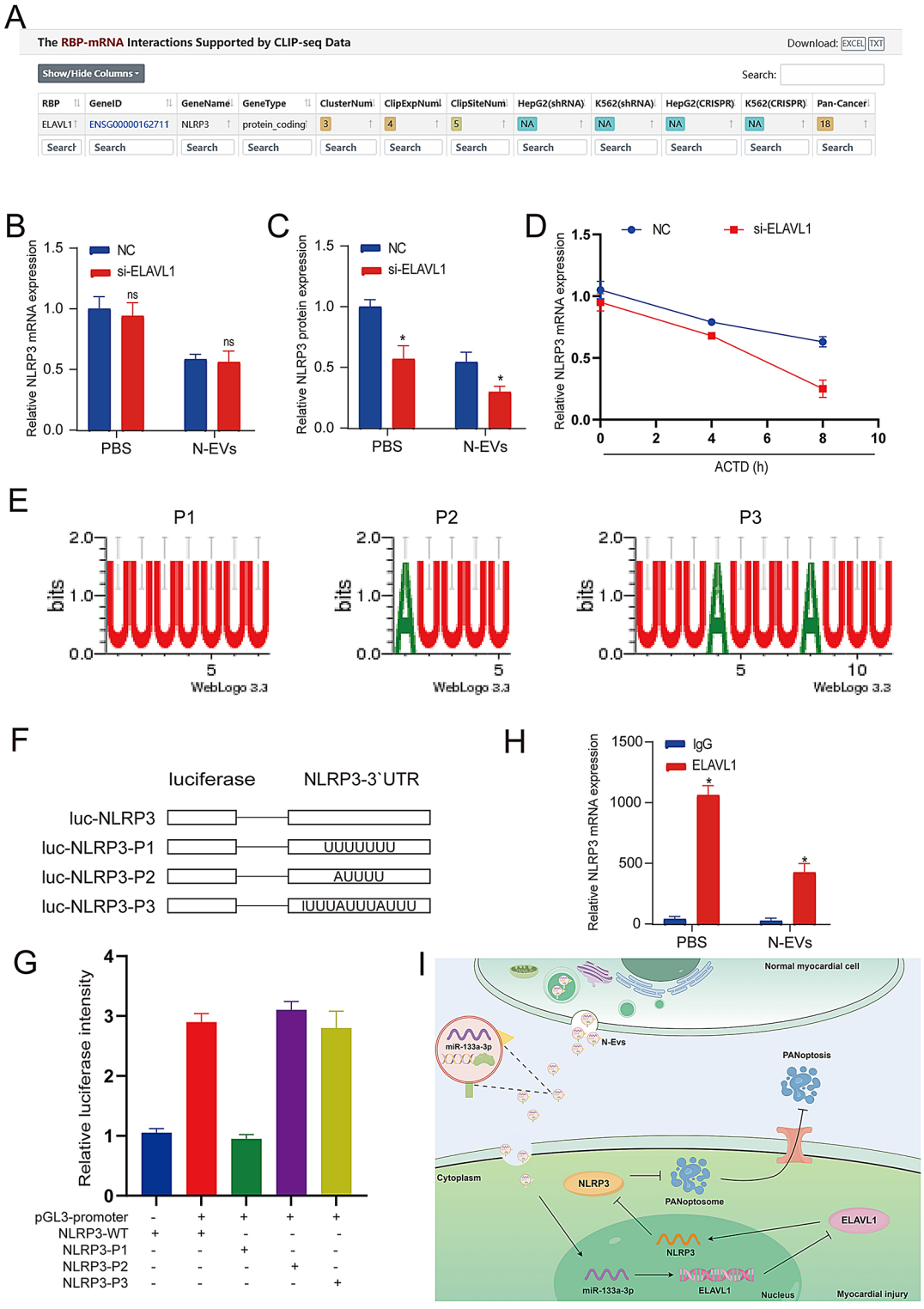

Fig. 7 (See legend on next page.)

is imperative for our research group to focus on developing comprehensive clinical studies in the future.

In summary, N-EVs deliver miR-133a-3p to inhibit the expression of ELAVL1 and NLRP3, preventing the formation of the PANoptosome and the occurrence of PANoptosis. This provides a novel therapeutic strategy for AMI. This finding not only deepens our understanding of the pathogenesis of AMI but also

(See figure on previous page.)

Fig. 7 ELAVL1 influences the formation of the PANoptosome by affecting the stability of NLRP3 mRNA. (**A**) The starBase database predicts the RBP protein of NLRP3. Legend: The starBase database was used to predict the RNA-binding proteins (RBPs) that interact with NLRP3 mRNA. The figure shows the predicted RBP proteins, with a focus on ELAVL1, which is known to play a role in mRNA stability and translation. The interaction scores and evidence from the database are provided to support the potential binding of ELAVL1 to NLRP3 mRNA. (**B**, **C**) QRT-PCR and WB were used to detect NLRP3 gene and protein expression ($P < 0.05$). Legend: (**B**) QRT-PCR was used to quantify the mRNA expression levels of NLRP3 in HUVEC and AC16 cells under different treatment conditions. Cells were treated with N-EVs (50 μg/mL), miR-133a-3p inhibitor (100 nM), or a combination of both for 24 h. The figure shows the relative mRNA expression levels of NLRP3, normalized to GAPDH. Legend: (**C**) Western blot analysis was used to examine the protein expression levels of NLRP3 in HUVEC and AC16 cells under different treatment conditions. Cells were treated with N-EVs (50 μg/mL), miR-133a-3p inhibitor (100nM), or a combination of both for 24 h. The figure shows the protein expression levels of NLRP3, with β-actin as the loading control. (**D**) RT-qPCR analysis of the decay rate of NLRP3 mRNA at the indicated times after ActD treatment. Legend: RT-qPCR was used to analyze the decay rate of NLRP3 mRNA in HUVEC and AC16 cells after treatment with actinomycin D (ActD, 5 μg/mL). Cells were treated with ActD for the indicated times (0, 2, 4, 6, and 8 h), and NLRP3 mRNA levels were quantified. The figure shows the relative mRNA levels of NLRP3 at each time point, normalized to GAPDH. (**E**) The ATtRACT database predicts ELAVL1 binding sites. Legend: The ATtRACT database was used to predict the binding sites of ELAVL1 on the NLRP3 mRNA. The figure shows the predicted binding sites within the 3'UTR of NLRP3 mRNA, highlighting the specific sequences and their positions. The binding scores and evidence from the database are provided to support the potential interaction between ELAVL1 and NLRP3 mRNA. (**F**, **G**) The targeting relationship between ELAVL1 and NLRP3 was confirmed by the dual-luciferase reporter assay. Legend: (**F**) The dual-luciferase reporter assay was used to confirm the direct targeting relationship between ELAVL1 and NLRP3. The 3'UTR of NLRP3 containing the putative ELAVL1 binding site was cloned into a luciferase reporter vector (NLRP3-WT). A mutant version of the 3'UTR with the binding site deleted (NLRP3-Mut) was also constructed. HEK293T cells were co-transfected with the reporter vectors and either ELAVL1 overexpression plasmid or a negative control (NC) plasmid. Luciferase activity was measured 48 h post-transfection. The figure shows the relative luciferase activity in the following groups: NC plasmid + NLRP3-WT, ELAVL1 overexpression plasmid + NLRP3-WT, NC plasmid + NLRP3-Mut, and ELAVL1 overexpression plasmid + NLRP3-Mut. Legend: (**G**) The dual-luciferase reporter assay was further used to confirm the targeting relationship between ELAVL1 and NLRP3 in the context of miR-133a-3p. HEK293T cells were co-transfected with the NLRP3-WT or NLRP3-Mut reporter vectors, ELAVL1 overexpression plasmid, and either miR-133a-3p mimic or a negative control (NC) mimic. Luciferase activity was measured 48 h post-transfection. The figure shows the relative luciferase activity in the following groups: NC mimic + NC plasmid + NLRP3-WT, miR-133a-3p mimic + NC plasmid + NLRP3-WT, NC mimic + ELAVL1 overexpression plasmid + NLRP3-WT, miR-133a-3p mimic + ELAVL1 overexpression plasmid + NLRP3-WT, NC mimic + NC plasmid + NLRP3-Mut, and miR-133a-3p mimic + NC plasmid + NLRP3-Mut. (**H**) RIP analysis of ELAVL1 protein binding to NLRP3 mRNA in cardiomyocytes. Legend: (**H**) RNA immunoprecipitation (RIP) assay was performed to validate the binding of ELAVL1 to NLRP3 mRNA in cardiomyocytes. Cardiomyocytes were lysed, and the cell lysates were incubated with magnetic beads conjugated with anti-ELAVL1 antibody or IgG (negative control). The enriched RNA was extracted and subjected to qRT-PCR to quantify the levels of NLRP3 mRNA. The figure shows the relative enrichment of NLRP3 mRNA in the ELAVL1-bound fraction compared to the IgG control. (**I**) Mechanism path diagram: Circulating extracellular vesicles regulate ELAVL1 by delivering miR-133a-3p, which affects NLRP3 mRNA stability, inhibiting PANoptosome formation. Legend: Schematic diagram illustrating the proposed mechanism by which circulating extracellular vesicles (EVs) regulate the expression and stability of NLRP3 mRNA through the delivery of miR-133a-3p. The diagram shows that N-EVs contain miR-133a-3p, which targets and reduces the expression of ELAVL1. Reduced ELAVL1 levels lead to decreased stability of NLRP3 mRNA, thereby inhibiting the formation of PANoptosomes and subsequent inflammatory responses

offers a theoretical basis for developing new treatment approaches. In conclusion, our findings demonstrate the pivotal role of circulating exosomes in facilitating intercellular communication through miR-133a-3p and their ability to regulate PANoptosis by targeting ELAVL1, thereby offering a potential therapeutic strategy for cardiomyocyte injury and fibrotic progression.

Abbreviations

AMI	Acute myocardial infarction
MIRI	Myocardial ischemia-reperfusion injury
EVs	Exosomes
HUVEC	Human umbilical vein endothelial cells
FBS	Fetal bovine serum
MI	Myocardial infarction
PBS	Phosphate-buffered saline
LVEF	Left ventricular ejection fraction

Supplementary Information

The online version contains supplementary material available at https://doi.org/10.1186/s13062-025-00605-2.

Supplementary Material 1: Supplementary Fig. 1 Characterization of EVs of different origins. (A) BCA was used to detect the total protein content of EVs from two different sources. Legend: Bicinchoninic acid (BCA) assay was used to measure the total protein content of EVs isolated from two different sources: N-EVs and AMI-Exo. The protein content was quantified and normalized to the volume of the isolated EVs. The figure shows the total protein content in μg/mL for each EV source. (B) The concentration of EVs secreted in each treatment group. Legend: The concentration of EVs secreted in each treatment group was measured using a nanoparticle tracking analysis (NTA). (C) WB was used to detect the expression of EVs markers from different sources. Legend: Western blot analysis was used to detect the expression of common EV markers (CD63, CD81, and TSG101) in EVs isolated from different sources: N-EVs and AMI-Exo. The figure shows the protein expression levels of these markers, with β-actin as the loading control. (D-E) Nanoparticle tracking analysis (NTA) and electron microscopy (EM) provide a better indication of EV size distribution and integrity. Legend: (D) Electron microscopy (EM) was used to visualize the morphology and integrity of EVs from different sources. Representative images of N-EVs and MSC-Exo are shown, with scale bars indicating the size of the EVs. The images demonstrate the typical cup-shaped morphology of EVs and their size range. Scale bar = 200 nm. Each group included 3 independent samples. Legend: (E) Nanoparticle tracking analysis (NTA) was used to determine the size distribution and concentration of EVs from different sources. The figure shows the size distribution histogram and the concentration of EV particles per mL for N-EVs and MSC-Exo.

Supplementary Material 2: Supplementary Fig. 2 The effect of miR-133a-3p content from different sources on cell proliferation. (A) PCR detection of miR-133a-3p expression levels in EVs derived from AMI and diabetic patients. Legend: Real-time quantitative PCR (QRT-PCR) was used to detect the expression levels of miR-133a-3p in extracellular vesicles (EVs) derived from acute myocardial infarction (AMI) patients and diabetic patients. The figure shows the relative expression levels of miR-133a-3p in the AMI group, diabetic group, and healthy control (Control) group. (B) EdU detection of the effect of EVs derived from AMI and diabetic patients on cell proliferation. Legend: 5-ethynyl-2'-deoxyuridine (EdU) staining was used to assess the effect of EVs derived from AMI and diabetic patients on cardiomyocyte proliferation. The figure shows the cell proliferation after treatment with EVs from the AMI group, diabetic group, and healthy

control (Control) group. The proportion of EdU-positive cells was observed and quantified using fluorescence microscopy. Data are presented as mean ± standard deviation (SD) from three independent experiments. Statistical significance was determined by one-way ANOVA followed by Tukey's multiple comparisons test, with $*P < 0.05$ indicating significant differences compared to the healthy control group, and $\#P < 0.05$ indicating significant differences compared to the diabetic group.

Supplementary Material 3: Supplementary Fig. 3 The effects of different miR on cell proliferation and apoptosis. (A) EdU detection of the effect of different treatments (PBS, N-EVs, N-EVs + miR-133a-3p inhibitor, N-EVs + miR-144-3p inhibitor, N-EVs + miR-23b-3p inhibitor) on cell proliferation. Legend: EdU staining was used to assess the effect of different treatments on cardiomyocyte proliferation. The treatments included PBS, N-EVs, N-EVs + miR-133a-3p inhibitor, N-EVs + miR-144-3p inhibitor, and N-EVs + miR-23b-3p inhibitor. The figure shows the proportion of EdU-positive cells, which indicates the proliferative capacity of the cardiomyocytes. Figure Description: EdU Staining: Fluorescence microscopy images showing EdU-positive cardiomyocytes after treatment with PBS, N-EVs, N-EVs + miR-133a-3p inhibitor, N-EVs + miR-144-3p inhibitor, and N-EVs + miR-23b-3p inhibitor. Quantification: Bar graph showing the proportion of EdU-positive cardiomyocytes after treatment with the different groups. Each bar represents the mean ± SD from three independent experiments. (B) Flow cytometry detection of the effect of different treatments (PBS, N-EVs, N-EVs + miR-133a-3p inhibitor, N-EVs + miR-144-3p inhibitor, N-EVs + miR-23b-3p inhibitor) on cell apoptosis. Legend: Flow cytometry was used to assess the effect of different treatments on cardiomyocyte apoptosis. The treatments included PBS, N-EVs, N-EVs + miR-133a-3p inhibitor, N-EVs + miR-144-3p inhibitor, and N-EVs + miR-23b-3p inhibitor. The figure shows the percentage of apoptotic cells, as determined by Annexin V/PI staining. Figure Description: Flow Cytometry: Dot plots showing the distribution of Annexin V/PI-stained cardiomyocytes after treatment with PBS, N-EVs, N-EVs + miR-133a-3p inhibitor, N-EVs + miR-144-3p inhibitor, and N-EVs + miR-23b-3p inhibitor. Quantification: Bar graph showing the percentage of apoptotic cardiomyocytes after treatment with the different groups. Each bar represents the mean ± SD from three independent experiments.

Supplementary Material 4: Supplementary Fig. 4 In vivo assays verified the role of PANoptosis in the treatment of myocardial injury by N-EVs. Legend: In vivo assays verified the role of PANoptosis in the treatment of myocardial injury by N-EVs. Real-time quantitative PCR (QRT-PCR) was used to detect the expression of PANoptosis-related markers in different treatment groups. The figure shows the mRNA expression levels of NLRP3, cleaved caspase-1, GSDMD in the Sham, PBS, N-EVs, and AMI-EVs groups. Data are presented as mean ± standard deviation (SD) from three independent experiments. Statistical significance was determined by one-way ANOVA followed by Tukey's multiple comparisons test, with $*P < 0.05$ indicating significant differences compared to the Sham group, and $\#P < 0.05$ indicating significant differences compared to the PBS group.

Supplementary Material 5: Supplementary Fig. 5 The expression of ELAVL1 in different treatment groups was detected by QRT-PCR and WB. Legend: The expression of ELAVL1 in different treatment groups was detected by real-time quantitative PCR (QRT-PCR) and Western blot (WB). QRT-PCR: The mRNA expression levels of ELAVL1 were measured in the PBS, N-EVs, and N-EVs + miR-133a-3p inhibitor groups. Western Blot: The protein expression levels of ELAVL1 were detected in the PBS, N-EVs, and N-EVs + miR-133a-3p inhibitor groups. β-actin was used as the loading control.

Supplementary Material 6: Supplementary Fig. 6 N-EVs effectively preserved cardiac function in rats with MI in vivo. (A) ELAVL1-positive stained capillaries in the border zone 4 weeks post-MI. Left ventricle was selected for the Sham group. Legend: ELAVL1-positive stained capillaries in the border zone 4 weeks post-MI. Immunofluorescence staining shows ELAVL1-positive capillaries in the left ventricular border zone. The Sham group was used for comparison. Scale bar = 100 μm. Each group included 5 animals. Representative images illustrate the distribution of ELAVL1-positive capillaries in each group. (B-D) Western blot analysis of PANoptosis-related protein expression. Legend: Western blot analysis of PANoptosis-related protein expression. Proteins detected include cleaved caspase-3 (apoptosis marker), cleaved caspase-1 (pyroptosis marker), GSDMD (pyroptosis marker), MLKL (necroptosis marker), and RIPK3 (necroptosis marker). β-actin was used as the loading control. Each group included 5 animals. Representative Western blot images show the protein expression levels in each group, and quantitative analysis was performed. Data are presented as mean ± standard error (SE) for continuous variables and percentages for categorical variables. Each group included 5 animals. Statistical significance was determined by two-way ANOVA followed by Bonferroni's multiple comparisons test, with $*P < 0.05$ indicating significant differences compared to the control group. The figure shows the mean values and error bars for LVEF and LVFS in the control and treatment groups at the specified time points.

Supplementary Material 7

Supplementary Material 8

Acknowledgements
Not applicable.

Author contributions
DlW and ZD made contribution to the Manuscript writing. LJ and KL provided the study materials. DlW and ZD analyzed and collected and assembled the data. LJ and KL made contribution to the conception and design. DlW and KL were responsible for the experiment and execution. All authors commented on previous versions of the manuscript. All authors read and approved the final manuscript.

Funding
This work was supported by the Sichuan Academy of Medical Sciences · Sichuan Provincial People's Hospital High-tech Project [No.30305030721].

Data availability
No datasets were generated or analysed during the current study.

Declarations

Ethics approval and consent to participate
All animal experiments were approved by the Animal Care and Use Committee of the Ethical Institution of Sichuan Provincial People's Hospital. The human study was approved by the Ethics Committee of Sichuan Provincial People's Hospital. Informed consent was obtained from all patient participants included in the study.

Consent for publication
The authors affirm that human research participants provided informed consent for publication.

Competing interests
The authors declare no competing interests.

Received: 26 August 2024 / Accepted: 13 January 2025
Published online: 26 March 2025

References

1. Zhu W, Sun L, Zhao P, Liu Y, Zhang J, Zhang Y, et al. Macrophage migration inhibitory factor facilitates the therapeutic efficacy of mesenchymal stem cells derived exosomes in acute myocardial infarction through upregulating miR-133a-3p. J Nanobiotechnol. 2021;19(1):61.
2. Zhang CS, Shao K, Liu CW, Li CJ, Yu BT. Hypoxic preconditioning BMSCs-exosomes inhibit cardiomyocyte apoptosis after acute myocardial infarction by upregulating microRNA-24. Eur Rev Med Pharmacol Sci. 2019;23(15):6691–9.
3. Wang L, Yang C, Chu M, Wang ZW, Xue B. Cdc20 induces the radioresistance of bladder cancer cells by targeting FoxO1 degradation. Cancer Lett. 2021;500:172–81.
4. Liang C, Liu Y, Xu H, Huang J, Shen Y, Chen F, et al. Exosomes of human umbilical cord MSCs protect against Hypoxia/Reoxygenation-Induced pyroptosis of Cardiomyocytes via the miRNA-100-5p/FOXO3/NLRP3 pathway. Front Bioeng Biotechnol. 2020;8:615850.
5. Huang L, Yang L, Ding Y, Jiang X, Xia Z, You Z. Human umbilical cord mesenchymal stem cells-derived exosomes transfers microRNA-19a to protect

cardiomyocytes from acute myocardial infarction by targeting SOX6. Cell Cycle. 2020;19(3):339–53.
6. Sun L, Zhu W, Zhao P, Wang Q, Fan B, Zhu Y, et al. Long noncoding RNA UCA1 from hypoxia-conditioned hMSC-derived exosomes: a novel molecular target for cardioprotection through miR-873-5p/XIAP axis. Cell Death Dis. 2020;11(8):696.
7. Taghdisi SM, Danesh NM, Ramezani M, Emrani AS, Abnous K. A novel electrochemical aptasensor based on Y-shape structure of dual-aptamer-complementary strand conjugate for ultrasensitive detection of myoglobin. Biosens Bioelectron. 2016;80:532–7.
8. Zheng M, Kanneganti TD. The regulation of the ZBP1-NLRP3 inflammasome and its implications in pyroptosis, apoptosis, and necroptosis (PANoptosis). Immunol Rev. 2020;297(1):26–38.
9. Samir P, Malireddi RKS, Kanneganti TD. The PANoptosome: a deadly protein complex driving pyroptosis, apoptosis, and necroptosis (PANoptosis). Front Cell Infect Microbiol. 2020;10:238.
10. Christgen S, Zheng M, Kesavardhana S, Karki R, Malireddi RKS, Banoth B, et al. Identification of the PANoptosome: a molecular platform triggering pyroptosis, apoptosis, and necroptosis (PANoptosis). Front Cell Infect Microbiol. 2020;10:237.
11. Zheng M, Karki R, Vogel P, Kanneganti TD. Caspase-6 is a Key Regulator of Innate Immunity, Inflammasome activation, and Host Defense. Cell. 2020;181(3):674–e8713.
12. Malireddi RKS, Kesavardhana S, Kanneganti TD. ZBP1 and TAK1: Master regulators of NLRP3 Inflammasome/Pyroptosis, apoptosis, and necroptosis (PAN-optosis). Front Cell Infect Microbiol. 2019;9:406.
13. Cao C, Wang B, Tang J, Zhao J, Guo J, Guo Q, et al. Circulating exosomes repair endothelial cell damage by delivering miR-193a-5p. J Cell Mol Med. 2021;25(4):2176–89.
14. Huang Y, Chen L, Feng Z, Chen W, Yan S, Yang R, et al. EPC-Derived exosomal miR-1246 and miR-1290 regulate phenotypic changes of fibroblasts to endothelial cells to Exert Protective effects on myocardial infarction by targeting ELF5 and SP1. Front Cell Dev Biol. 2021;9:647763.
15. Liao Z, Chen Y, Duan C, Zhu K, Huang R, Zhao H, et al. Cardiac telocytes inhibit cardiac microvascular endothelial cell apoptosis through exosomal miRNA-21-5p-targeted cdip1 silencing to improve angiogenesis following myocardial infarction. Theranostics. 2021;11(1):268–91.
16. Yan F, Chen Y, Ye X, Zhang F, Wang S, Zhang L, et al. miR-3113-5p, miR-223-3p, miR-133a-3p, and miR-499a-5p are sensitive biomarkers to diagnose sudden cardiac death. Diagn Pathol. 2021;16(1):67.
17. Kuzmin VS, Ivanova AD, Filatova TS, Pustovit KB, Kobylina AA, Atkinson AJ, et al. Micro-RNA 133a-3p induces repolarization abnormalities in atrial myocardium and modulates ventricular electrophysiology affecting I(ca,L) and Ito currents. Eur J Pharmacol. 2021;908:174369.
18. Li M, Ding W, Tariq MA, Chang W, Zhang X, Xu W, et al. A circular transcript of ncx1 gene mediates ischemic myocardial injury by targeting miR-133a-3p. Theranostics. 2018;8(21):5855–69.
19. Liu N, Zhen Z, Xiong X, Xue Y. Aerobic exercise protects MI heart through miR-133a-3p downregulation of connective tissue growth factor. PLoS ONE. 2024;19(1):e0296430.
20. Bian Y, Li X, Pang P, Hu XL, Yu ST, Liu YN, et al. Kanglexin, a novel anthraquinone compound, protects against myocardial ischemic injury in mice by suppressing NLRP3 and pyroptosis. Acta Pharmacol Sin. 2020;41(3):319–26.
21. Chen A, Chen Z, Zhou Y, Wu Y, Xia Y, Lu D, et al. Rosuvastatin protects against coronary microembolization-induced cardiac injury via inhibiting NLRP3 inflammasome activation. Cell Death Dis. 2021;12(1):78.
22. Lv J, Hao YN, Wang XP, Lu WH, Xie LY, Niu D. Bone marrow mesenchymal stem cell-derived exosomal miR-30e-5p ameliorates high-glucose induced renal proximal tubular cell pyroptosis by inhibiting ELAVL1. Ren Fail. 2023;45(1):2177082.
23. Zhu B, He J, Ye X, Pei X, Bai Y, Gao F, et al. Role of cisplatin in inducing Acute kidney Injury and pyroptosis in mice via the Exosome miR-122/ELAVL1 Regulatory Axis. Physiol Res. 2023;72(6):753–65.
24. Huang T, Ding J, Lin L, Han L, Yu L, Li M. Bioinformatic identification of the Pyroptosis-Related Transcription Factor-MicroRNA-Target Gene Regulatory Network in Angiotensin II-Induced Cardiac Remodeling and Validation of Key Components. Front Biosci (Landmark Ed). 2023;28(11):293.
25. Jeyabal P, Thandavarayan RA, Joladarashi D, Suresh Babu S, Krishnamurthy S, Bhimaraj A, et al. MicroRNA-9 inhibits hyperglycemia-induced pyroptosis in human ventricular cardiomyocytes by targeting ELAVL1. Biochem Biophys Res Commun. 2016;471(4):423–9.
26. Jiang Y, Ge W, Zhao Y, Wu Y, Huo Y, Pan L, et al. [LINC00926 promotes pyroptosis of hypoxia-induced human umbilical vein vascular endothelial cells by recruiting ELAVL1]. Nan Fang Yi Ke Da Xue Xue Bao. 2023;43(5):807–14.
27. Liu N, Xie L, Xiao P, Chen X, Kong W, Lou Q, et al. Cardiac fibroblasts secrete exosome microRNA to suppress cardiomyocyte pyroptosis in myocardial ischemia/reperfusion injury. Mol Cell Biochem. 2022;477(4):1249–60.
28. Cui Y, Wang X, Lin F, Li W, Zhao Y, Zhu F, et al. MiR-29a-3p improves Acute Lung Injury by reducing alveolar epithelial cell PANoptosis. Aging Dis. 2022;13(3):899–909.
29. Zhang W, Xia CL, Qu YD, Li JX, Liu JB, Ou SJ, et al. MicroRNA-18a regulates the pyroptosis, apoptosis, and necroptosis (PANoptosis) of osteoblasts induced by tumor necrosis factor-α via hypoxia-inducible factor-1α. Int Immunopharmacol. 2024;128:111453.
30. Yang X, Xu J, Lan S, Tong Z, Chen K, Liu Z, et al. Exosomal miR-133a-3p derived from BMSCs alleviates cerebral ischemia-reperfusion Injury via Targeting DAPK2. Int J Nanomed. 2023;18:65–78.
31. Zhu YF, Wang R, Chen W, Cao YD, Li LP, Chen X. miR-133a-3p attenuates cardiomyocyte hypertrophy through inhibiting pyroptosis activation by targeting IKKε. Acta Histochem. 2021;123(1):151653.
32. Guo H, Wang Y, Jia W, Liu L. MiR-133a-3p relieves the oxidative stress induced trophoblast cell apoptosis through the BACH1/Nrf2/HO-1 signaling pathway. Physiol Res. 2021;70(1):67–78.

Publisher's note